Helicopter Rotor Optimization via Operator Overloading-Based Discrete Adjoint Approach

Reza Djeddi* and Kivanc Ekici†

University of Tennessee, Knoxville, Tennessee 37996

A memory efficient framework is developed for the aerodynamic design optimization of helicopter rotor blades in hover. This framework is based on a fully-automated discrete-adjoint toolbox called FDOT. The in-house toolbox is capable of computing sensitivity or gradient information very accurately, and uses an operator-overloading technique that takes advantage of a unique expression-template-based approach for memory and computational efficiency while still being fully-automated with minimal user interventions. The main goal of the present work is to "design" helicopter rotor blades with increased figure-of-merit. Therefore, the flow around the Caradonna-Tung rotor in non-lifting and lifting hover conditions is studied in order to validate the primal and adjoint solvers based on a rotating frame of reference formulation. The efficacy of the optimization framework is first demonstrated for drag minimization of a rotating NACA 0012 airfoil, which resembles a Vertical-Axis Wind Turbine (VAWT) configuration. Finally, the single- and multi-point design optimization results for the Caradonna-Tung rotor are presented. It is important to note that the current approach (FDOT) can be directly coupled – in a "black-box" manner – to other existing codes in the Helios computational platform, which is part of CREATE-AV.

I. Introduction

The design of helicopter rotor blades is a very complex and demanding task. The prediction of helicopter rotor performance in both hover and forward flight depends heavily on accurate prediction of transonic flows and proper resolution of the blade-vortex as well as the blade-wake interactions. In particular, the flow around the rotor blades differs significantly from that of the fixed wings due to the linear variation of the local velocities along the rotor blade with the distance from the hub. Therefore, subsonic to transonic flow regimes can occur at the same time along the rotor blade which would require the utilization of a robust compressible flow solver. In the past few decades, many research efforts have focused on helicopter rotor modeling with various fidelity ranging from potential flow solvers[1,2] to Euler and Reynolds-Averaged Navier-Stokes (RANS) calculations.[3–6]

In general, it is necessary to solve unsteady governing equations for fluid dynamics when studying flows around rotor blades. For a helicopter rotor in hover, however, one can utilize a "rotating frame of reference (RFR)" where the coordinate system is established on the blades and rotates with the rotor. Therefore, in the case of the steady rotation, it is possible to solve the "steady" governing equations written in rotating frame instead of the unsteady equations in the inertial frame of reference.[3] As a result, the computational cost of unsteady Euler or URANS simulations will be greatly reduced. For the forward flight conditions, however, the flow can no longer be viewed as steady in the rotating frame due to the completely different dynamics of the fluid around advancing and retreating blades. It must be noted that researchers have also utilized time-spectral methods to study the forward flight dynamics of a helicopter rotor that can greatly improve the computational efficiency due to a *mathematically steady* reformulation of the governing equations.[7–9]

With the advances in computing resources, the aerodynamic design optimization (ADO) has attracted many researchers to focus on improving the aerodynamic systems with optimized topologies that satisfy

*Research Assistant Professor and Lecturer, Department of Mechanical, Aerospace and Biomedical Engineering, Professional Member AIAA.

†Professor, Department of Mechanical, Aerospace and Biomedical Engineering, Senior Member AIAA.

certain aeromechanical objectives. In particular, gradient-based design optimization techniques, that rely on accurate gradient or sensitivity information, have grown in popularity. Unlike stochastic methods, such as simulated annealing and genetic algorithms, gradient-based optimization methods can sometimes get trapped in a local optimum. Nevertheless, these methods are highly reliable in converging to a local optima in very few design cycles. This characteristic, makes gradient-based techniques highly attractive for aerodynamic design optimization of fixed wing aircraft and rotorcraft due to the high computational cost associated with each functional evaluation.

While research has prominently matured in the field of design optimization for fixed-wing or even full aircraft configurations, fewer efforts were reported on the aerodynamic shape optimization of helicopter rotor blades.[10–12] Le Pape and Beaumier[13] have used a gradient-based minimization tool with the three-dimensional Navier-Stokes CFD solver *elsA* to optimize rotors in hover. Kriging interpolation models within a design of experiment (DOE) framework based on smooth surrogate models have also been utilized by Vu et al.[14] to minimize the required power for hovering state of a Bo 105 LS helicopter blade section. Generally, aerodynamic design optimization involves high-dimensional design spaces with tens to thousands of design variables. This means that the finite-difference approach for gradient calculation would not be a suitable choice. Despite the high computational cost, Morris et al.[15] have proposed a generic optimization tool for high-fidelity aerodynamic design of rotor blades that utilizes finite-differences for gradient-based optimization. Nevertheless, adjoint methods,[16,17] whose computational cost in calculating the gradient information is theoretically independent from the number of design variables, are more often the obvious choice in such applications.

The adjoint method can be implemented in two different forms depending on the order with which the discretization and variation steps are performed. In the "continuous" adjoint approach[18,19] the variation of the governing equations is taken first before discretizing the resulting set of equations. As an example to this approach, Lee and Kwon[20] utilized a continuous adjoint approach for redesigning Caradonna-Tung-[21] and UH-60- rotors while also using a solution-adaptive mesh refinement method to improve the resolution of the blade's tip vortex. An alternative to the continuous adjoint technique is the "discrete" adjoint approach[22,23] where the order of discretization and variation would be reversed. Tatossian et al.[9] presented discrete adjoint-based aerodynamic design optimization of helicopter rotor blades in hover using a Non-Linear Frequency Domain (NLFD) technique. Of particular interest in the present work is the discrete adjoint method where the cost function is first augmented with the flow equations – using the Lagrange multipliers – before taking their variations. The latter step is generally accomplished using automatic or algorithmic differentiation (AD) which systematically applies the chain rule of differentiation to the discretized equations. Interested reader is referred to Ref.[24] for further details on various gradient calculation techniques.

In the literature, aerodynamic design studies have often focused on "single-point" optimization where the optimal design is achieved for a specific flow condition. While providing significant improvements at the target flow condition, such applications are prone to exhibit poor off-design performance. As an example, a single-point optimization of the NASA Common Research Model (CRM)[25] can lead to significant reductions of the drag count at the cruise conditions while performing poorly at landing/take-off conditions.[26] Therefore, a new class of "multi-point" optimization techniques are introduced that can search the design space over the complete flight operating envelope. In recent years, many research efforts have utilized such multi-point optimization techniques for the design of airfoils,[27,28] fixed wings and aircraft configurations,[26,29,30] as well as in turbomachinery applications.[31–34] However, to the best of the authors' knowledge, the present work is the first application of a multi-point optimization technique for the design of helicopter rotor blades in hover conditions.

In this paper, a robust tool for aerodynamic design of helicopter rotor blades is developed. The framework couples an in-house primal CFD solver with an in-house automatic differentiation (AD) toolbox for an efficient and fully-automated design optimization.[35] The compressible Reynolds-Averaged Navier-Stokes (RANS) solver (**UNPAC**)[24,36] uses a rotating frame of reference formulation of the governing equations including the additional source terms due to centrifugal and Coriolis forces. Additionally, the discrete adjoint-based automatic differentiation toolbox (**FDOT**), originally developed by the authors,[37,38] provides highly accurate sensitivity information required for the gradient-based design optimization. The AD toolbox is enhanced with an expression-template-based approach that can provide memory and computational efficiency while still being fully-automated with minimal changes required to the primal solver. The goal of the present work is to utilize the developed optimization framework (**UNPAC-DOF**) for improving the helicopter rotor blade design in hover to maximize thrust and minimize torque at various rotational speeds in a multi-point

optimization approach. In the following sections, details of the primal and adjoint flow solvers as well as the design optimization framework are presented. Initially, the primal and adjoint solutions are validated for the Caradonna-Tung rotor[21] in non-lifting and lifting hover conditions with various rotational speeds and collective pitch angles. Next, the framework is utilized for the single- and multi-point drag minimization of a rotating NACA 0012 airfoil. Finally, the proposed technique is extended to a multi-point aerodynamic shape optimization of the Caradonna-Tung rotor at various rotational speeds with a fixed pitch angle. It is worth noting that the current approach to compute adjoint sensitivities using FDOT can be directly coupled in a "black-box" manner with other existing codes in the Helios computational platform, which is part of CREATE-AV.

II. Multi-Point Design Optimization Framework for Helicopter Rotor Blades

The computational framework that handles the single- and multi-point design optimization tasks is described in this section. As discussed earlier, this framework couples both of our in-house flow solver and AD tools to obtain primal and adjoint flow solutions. Ultimately, the objective and gradient information are provided to the optimizer algorithm to update the design for the next cycle.

A. Primal Flow Solver

The flow solver used in this work models the three-dimensional URANS equations fully coupled with the Spalart-Allmaras turbulence model.[39] In general, the governing equations are written in the differential form for the "interial frame of reference" as

$$\frac{\partial \mathbf{U}}{\partial t} + \frac{\partial \left(\mathbf{F_c} - \mathbf{F_v}\right)}{\partial x} + \frac{\partial \left(\mathbf{G_c} - \mathbf{G}_v\right)}{\partial y} + \frac{\partial \left(\mathbf{H_c} - \mathbf{H_v}\right)}{\partial z} = \mathbf{S} \tag{1}$$

where the vector of conservative variables is $\mathbf{U} = [\rho, \rho u, \rho v, \rho w, \rho E, \rho\tilde{\nu}]^T$ and the vectors of convective, $(\mathbf{F_c}, \mathbf{G_c}, \mathbf{H_c})$, and viscous, $(\mathbf{F_v}, \mathbf{G_v}, \mathbf{H_v})$, fluxes in three Cartesian directions as well as the source terms are given as:

$$\mathbf{F_c} = \begin{bmatrix} \rho u \\ \rho u^2 + p \\ \rho uv \\ \rho uw \\ \rho uH \\ \rho u\tilde{\nu} \end{bmatrix}, \ \mathbf{G_c} = \begin{bmatrix} \rho v \\ \rho uv \\ \rho v^2 + p \\ \rho vw \\ \rho vH \\ \rho v\tilde{\nu} \end{bmatrix}, \ \mathbf{H_c} = \begin{bmatrix} \rho w \\ \rho wu \\ \rho wv \\ \rho w^2 + p \\ \rho wH \\ \rho w\tilde{\nu} \end{bmatrix}$$

$$\mathbf{F_v} = \begin{bmatrix} 0 \\ \tau_{xx} \\ \tau_{xy} \\ \tau_{xz} \\ \tau_{xh} \\ \tau_{x\tilde{\nu}} \end{bmatrix}, \ \mathbf{G_v} = \begin{bmatrix} 0 \\ \tau_{yx} \\ \tau_{yy} \\ \tau_{yz} \\ \tau_{yh} \\ \tau_{y\tilde{\nu}} \end{bmatrix}, \ \mathbf{H_v} = \begin{bmatrix} 0 \\ \tau_{zx} \\ \tau_{zy} \\ \tau_{zz} \\ \tau_{zh} \\ \tau_{z\tilde{\nu}} \end{bmatrix}, \ \mathbf{S} = \begin{bmatrix} 0 \\ 0 \\ 0 \\ 0 \\ 0 \\ S_{\mathrm{SA}} \end{bmatrix}$$

Here, $\tilde{\nu}$ is the viscosity-like working variable of the Spalart-Allmaras turbulence model and S_{SA} is the source term of the Spalart-Allmaras turbulence model.[39] The pressure, p, and the total enthalpy, H, are defined in terms of the conservative variables as

$$p = (\gamma - 1)\rho\left[E - \frac{1}{2}(u^2 + v^2 + w^2)\right]$$

$$H = \frac{\rho E + p}{\rho} = \frac{\gamma}{\gamma - 1}\frac{p}{\rho} + \frac{1}{2}(u^2 + v^2 + w^2)$$

In the case of the steady rotation with angular velocity Ω, the governing equations described in Eq. (1), can be written in a rotating frame of reference instead of the inertial frame. The rotation of the Cartesian reference frame with the rotor will introduce relative and rotational velocities described as

$$u = u_r - u_\Omega, \quad v = v_r - v_\Omega, \quad w = w_r - w_\Omega \tag{2}$$

where (u_r, v_r, w_r) and $(u_\Omega, v_\Omega, w_\Omega)$ are the relative and rotational velocity components, respectively. Let us assume a hovering helicopter rotor with a uniform rotation rate Ω about the y-axis. Therefore, rotational velocity components can be defined as

$$u_\Omega = -\Omega z, \quad v_\Omega = 0, \quad w_\Omega = \Omega x \tag{3}$$

In this work, we use an approach similar to that proposed by Agarwal and Deese[3] where the governing equations in relative frame of reference are recast in terms of absolute flow variables to simplify the implementation of the far-field boundary conditions. Therefore, the governing equations for the rotating case can be re-written as:

$$\frac{\partial \mathbf{U}}{\partial t} + \frac{\partial \left(\mathbf{F_c} - \mathbf{F_v}\right)}{\partial x} + \frac{\partial \left(\mathbf{G_c} - \mathbf{G}_v\right)}{\partial y} + \frac{\partial \left(\mathbf{H_c} - \mathbf{H_v}\right)}{\partial z} + u_\Omega \frac{\partial \mathbf{U}}{\partial x} + v_\Omega \frac{\partial \mathbf{U}}{\partial y} + w_\Omega \frac{\partial \mathbf{U}}{\partial z} = \underline{\mathbf{S}} \tag{4}$$

where $\underline{\mathbf{S}}$ is the modified vector of source terms which now also includes terms due to the centrifugal and Coriolis forces.[24] For the specific case of uniform rotation with angular velocity Ω about the y-axis, the vector of source terms for our 3D RANS solver can be defined as

$$\underline{\mathbf{S}} = \begin{bmatrix} 0 \\ -\rho\Omega w \\ 0 \\ \rho\Omega u \\ 0 \\ S_{\mathrm{SA}} \end{bmatrix} \tag{5}$$

The governing equations given in Eq. (4) are discretized using a finite volume method with median-dual, vertex-based control volume approach.[24,36,40] Also, for steady cases, the time-derivative term is replaced with a *pseudo-time* derivative in order to march the governing equations to steady-state. Therefore, the semi-discretized form of the governing equations can be written as

$$\frac{d}{d\tau}\left(\mathcal{V}\mathbf{U}\right) + \mathbf{R}(\mathbf{U}) = \mathbf{0} \tag{6}$$

where $\mathcal{V}$ is the control volume, τ is the pseudo-time, and $\mathbf{R}$ is the residual that represents the discretization of the spatial terms that include both the convective fluxes and viscous fluxes as well as the turbulence model and rotating frame of reference source terms. The convective terms are discretized using an upwind scheme based on Roe-fluxes.[41] Additionally, limiter functions of Barth and Jespersen[42] and Venkatakrishnan[43] are used for the upwind convective fluxes in the case of higher-order solution reconstruction at the face center. A second-order central averaging scheme is used for the calculation of the viscous fluxes. The gradients of the flow variables are calculated at the grid nodes using a Green-Gauss method. Furthermore, the solver is parallelized using the message passing interface (MPI) tools with a non-overlapping domain decomposition,[44] and METIS software package[45] is used for partitioning the computational domain.

B. Adjoint Flow Solver

In this section, details about the fully-automated discrete adjoint toolbox (FDOT) are provided. It must be noted that the original idea was introduced by the authors in a previous publication[37] and further developed in a subsequent work[38] using a memory efficient expression-template-based approach. As such, the theory is repeated here for completeness, and it closely follows the work presented in Refs.[37,38] The goal of the aerodynamic design optimization process is to find the optimal solution (or design) that can minimize the objective function, $I(\mathbf{x}, \mathbf{U}(\mathbf{x}))$, defined in terms of the design variables, $\mathbf{x}$, and the corresponding flow solution, $\mathbf{U}(\mathbf{x})$. As discussed earlier, in the framework of a gradient-based design optimization problem, the gradient of the objective function with respect to the design variables is required. This gradient can be written as the total derivative of the objective function with respect to the design variables:

$$\frac{dI}{d\mathbf{x}} = \frac{\partial I}{\partial \mathbf{x}} + \frac{\partial I}{\partial \mathbf{U}} \frac{\partial \mathbf{U}}{\partial \mathbf{x}} \tag{7}$$

where $\mathbf{x}$ is the vector of design variables. In an Aerodynamic Shape Optimization (ASO) problem, the objective function is usually defined as a scalar integrated quantity (drag, thrust, or torque coefficient) while the number of design variables can be on the order of $\mathcal{O}(10)$ to $\mathcal{O}(10^2)$ for a two- or three-dimensional problem. On the other hand, the size of the $\mathbf{U}$ vector or the number of degrees of freedom (DOF) for a typical CFD solver can easily be on the order of $\mathcal{O}(10^5)$ to $\mathcal{O}(10^7)$. As a result, evaluating the Jacobian term, $\frac{\partial \mathbf{U}}{\partial \mathbf{x}}$, in Eq. (7) can become prohibitively expensive. Therefore, it would be impractical to use a direct approach in sensitivity analysis. It must be noted that the flow solution and the corresponding flow residual (see Eq. [6]) are both defined in terms of the design variables for an ASO problem. Thus, Eq. (6) can be rewritten as

$$\frac{d}{dt}\left(\mathcal{V}\mathbf{U}(\mathbf{x})\right) + \mathbf{R}(\mathbf{x}, \mathbf{U}(\mathbf{x})) = \mathbf{0}. \tag{8}$$

In practice, the converged steady solution for any CFD solver means that the residual vector is driven to zero. Moreover, it can be assumed that the total derivative of the residual vector with respect to the vector of design variables would also vanish when the solution is converged, i.e.,

$$\frac{d\mathbf{R}}{d\mathbf{x}} = \frac{\partial \mathbf{R}}{\partial \mathbf{x}} + \frac{\partial \mathbf{R}}{\partial \mathbf{U}}\frac{\partial \mathbf{U}}{\partial \mathbf{x}} = \mathbf{0} \tag{9}$$

By rearranging Eq. (9) and inserting it into Eq. (7), the total derivative of the objective function with respect to the design variables can be rewritten as

$$\frac{dI}{d\mathbf{x}} = \frac{\partial I}{\partial \mathbf{x}} - \frac{\partial I}{\partial \mathbf{U}}\left[\frac{\partial \mathbf{R}}{\partial \mathbf{U}}\right]^{-1}\frac{\partial \mathbf{R}}{\partial \mathbf{x}} = \frac{\partial I}{\partial \mathbf{x}} + \psi^T\frac{\partial \mathbf{R}}{\partial \mathbf{x}} \tag{10}$$

where ψ is the adjoint solution vector. Calculating the adjoint solution vector is the essence of both discrete and continuous adjoint approaches. The main goal here is to efficiently and accurately evaluate all the partial derivatives in Eq. (10) in order to find the necessary gradient information for the ASO problem.

The FDOT toolbox developed by Djeddi and Ekici[37] utilizes the concept of discrete adjoint sensitivity analysis and the object-oriented programming (OOP) capabilities of the modern Fortran programming language to evaluate the gradient information. By defining a new derived type for real-typed variables and by overloading all the unary and binary operations and intrinsic functions, the FDOT toolbox can be coupled with any numerical solver to provide the sensitivities (gradients) of the output (objective) function(s) with respect to all design variables. Calculating these gradients is done via an "adjoint evaluation" process whose computational cost is only a small multiple of that of the primal solver.[46,47] The FDOT toolbox uses a fixed-point iteration approach, as originally proposed by Christianson,[48,49] coupled with a "checkpointing" process to improve the computational efficiency in evaluating the adjoint solutions. Additionally, the AD toolbox takes advantage of a novel expression-template-based technique,[38] that can greatly enhance the memory efficiency while still providing a fully-automated adjoint sensitivity analysis. After obtaining the adjoint solutions, the calculated sensitivity information will be used for gradient-based design optimization which will be described next.

C. Design Optimization Process

Traditionally, aerodynamic design process has heavily relied on experimental wind tunnel tests and engineering judgment. With the advent of computational fluid dynamics, numerical shape optimization has been made possible without expensive and cost-prohibitive experiments and wind tunnel tests. Over the years, robust design methodologies have been proposed in aerodynamic shape optimization. Additionally, a whole field has been devoted to developing algorithms and black-box software packages used for numerical optimization.[50]

As discussed earlier, the gradient-based optimization approach is considered in this work. The UNPAC solver is used to obtain primal (or flow) solutions. Furthermore, the FDOT toolbox and the CFD code are integrated into the UNPAC-AD framework to compute the gradient information. Finally, the UNPAC-OPT wrapper program is developed to perform design optimization.[24] Simply, UNPAC-OPT uses a quasi-Newton method for optimization in both unbounded and bound constrained modes subject to upper and/or lower bounds for the design variables.

1. *Single-Point Optimization*

A very common approach in aerodynamic design optimization is to optimize the performance at one specific point in the design space which can correspond to a single flight condition. In such cases, the goal is to minimize the objective function via

$$\begin{aligned} \min \quad & I(\mathbf{x}, \mathbf{U}(\mathbf{x})) \\ \text{w.r.t} \quad & \mathbf{x} \\ \text{subject to} \quad & \mathbf{R}(\mathbf{U}(\mathbf{x})) = 0 \end{aligned} \tag{11}$$

For a single-point optimization, the objective function can be defined simply as the drag coefficient, or in the case of a helicopter rotor, the Figure of Merit (FM) defined as

$$\text{FM} = \frac{C_T^{3/2}}{\sqrt{2} C_Q} \tag{12}$$

where C_T and C_Q are the thrust and torque coefficients, respectively. It must be noted that the optimization problem normally seeks to minimize the objective function. While this would be the case for a design optimization based on the drag coefficient as the objective function, the Figure of Merit needs to be maximized. Therefore, a simplistic approach would be to set the objective function as either $I = -\text{FM}$ or $I = 1/\text{FM}$ with the goal of maximizing the thrust coefficient while minimizing the torque.[51] However, numerical results have shown that this approach would normally increase the figure of merit by increasing both thrust and torque coefficients which can potentially lead to a worse overall design that has a lower thrust-to-torque ratio. Therefore, in this work, a thrust-constrained torque minimization approach is utilized that can effectively lead to an increase in the figure of merit without losses in thrust-to-torque ratio. In this work, a penalty function approach is used for the "inequality constrained" optimization problem such that the following objective is considered for the minimization problem defined in Eq. (11)

$$I = C_Q + \gamma_p \, p^+ \left(C_T, C_{T,\min} \right) \tag{13}$$

where p^+ is the penalty function defined as

$$p^+ \left(C_T, C_{T,\min} \right) = \begin{cases} 0 & C_T \geq C_{T,\min} \\ \left(C_T - C_{T,\min} \right)^2 & C_T < C_{T,\min} \end{cases} \tag{14}$$

where $C_{T,\min}$ is the minimum thrust coefficient that needs to be maintained during the torque minimization process. Additionally, γ_p is the regularization or penalty factor which is taken to be $\gamma_p = 1.5 \times 10^4$ for the constrained optimization problem studied in this work involving the Caradonna and Tung rotor. It must be noted that both of the objective functions, i.e., the drag coefficient or the thrust-constrained torque coefficient, will be defined at a single flight condition. For example, in the case of the helicopter rotor design, the thrust and torque coefficients will be defined at a specific pitch angle and rotational speed (or tip Mach number).

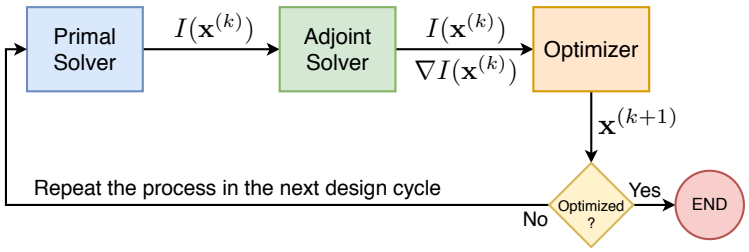

Figure 1. Flowchart of the single-point design optimization process.

A schematic of the standard gradient-based design optimization process is shown in Fig. (1). The optimization framework seeks optimal designs via an iterative process in which the following steps are considered for each design cycle k

1. The primal CFD solver (UNPAC) is run to obtain the flow solution. After obtaining the flow solution, the value of the objective function at the current design, $I(\mathbf{x}^{(k)})$, will be calculated.

2. Using the primal flow solution, the adjoint solver (UNPAC-AD) is initiated. After convergence, the adjoint solution is used to calculate the sensitivity information for the objective function with respect to the set of design variables, i.e., $\nabla I(\mathbf{x}^{(k)})$.

3. The objective function and the gradient information are then input into the UNPAC-OPT program. Here, the gradient information is passed on to a quasi-Newton optimizer to obtain the new set of design variables $\mathbf{x}^{(k+1)}$.

4. The new set of design variables will mean a new topology in the case of the aerodynamic shape optimization. This new topology is then returned back to the UNPAC solver to deform the surface and volume meshes for the next design cycle. The optimization process is repeated until either the desired number of design cycles is reached or the desired tolerance for the optimal solution has been achieved.

2. Multi-Point Optimization

As discussed previously, an important issue with the single-point aerodynamic design optimization is the possible performance penalty suffered by the same design at other flight conditions. Therefore, a good comprise between multiple flight conditions in the design space would be to use a multi-point aerodynamic design optimization. For the case of rotor optimization, the objective may involve different flight conditions. Therefore, the objective function for the multi-point optimization can be defined as

$$I_{\text{MP}} = \beta_1 I_1 + \beta_2 I_2 + \beta_3 I_3 + \cdots + \beta_p I_p \tag{15}$$

where we seek to minimize the multi-point objective I_{MP} over p different flight conditions. A similar approach has been proposed by Leoviriyakit and Jameson[29] for the multi-point design of a wing planform with drag and structural weight considerations. Choice of weights β for the multi-point objective function depends on the importance of each individual flight condition with the sum of all weights being equal to one,[29] i.e.,

$$\beta_1 + \beta_2 + \beta_3 + \cdots + \beta_p = 1.0 \tag{16}$$

Ultimately, the gradient or sensitivity of the multi-point objective function with respect to the set of design variables can be also found via

$$\nabla I_{\text{MP}} = \beta_1 \nabla I_1 + \beta_2 \nabla I_2 + \beta_3 \nabla I_3 + \cdots + \beta_p \nabla I_p \tag{17}$$

Similar to the single-point design optimization, the global objective function and its gradient information are passed to a gradient-based optimizer (in our case the L-BFGS-B[52] or the SLSQP[53] algorithms) to obtain the new set of design variables. This process is repeated until the required minimization of the objective function is achieved according to the schematic of the multi-point optimization shown in Fig. (2).

III. Solver Validation and Verification: Caradonna-Tung Rotor in Hover

In this section, the flow past a helicopter rotor in hover is studied to validate the primal and adjoint flow solutions. This step is crucial in any ASO study to ensure the efficacy of the optimization framework. Based on the experiments carried out by Caradonna and Tung,[21] the rotor geometry consists of two untapered and untwisted blades with NACA0012 profile. To validate the three-dimensional UNPAC solver based on the rotating frame of reference, three different operating conditions are considered with details provided in Table (1). As can be seen, for the non-lifting case, the collective pitch angle as well as the pre-cone angle are both zero with the tip Mach number set to 0.52. Additionally, two lifting cases in hover condition are considered with a collective pitch angle of 8-deg and a 0.5-deg pre-cone angle. It must be noted that in all of these cases, the rotor blades have an aspect ratio of 6 and the chord length is $c = 0.1905$ units.[21] The axis of rotation is aligned with the z-axis. Additionally, since the rotor is in hover mode, the free-stream Mach number in the inertial frame of reference is zero.

For all three cases presented in this section, a semi-cylindrical computational domain is used with the periodic boundaries located at $y = 0$ plane and the domain is extended for 12 chord lengths in the radial

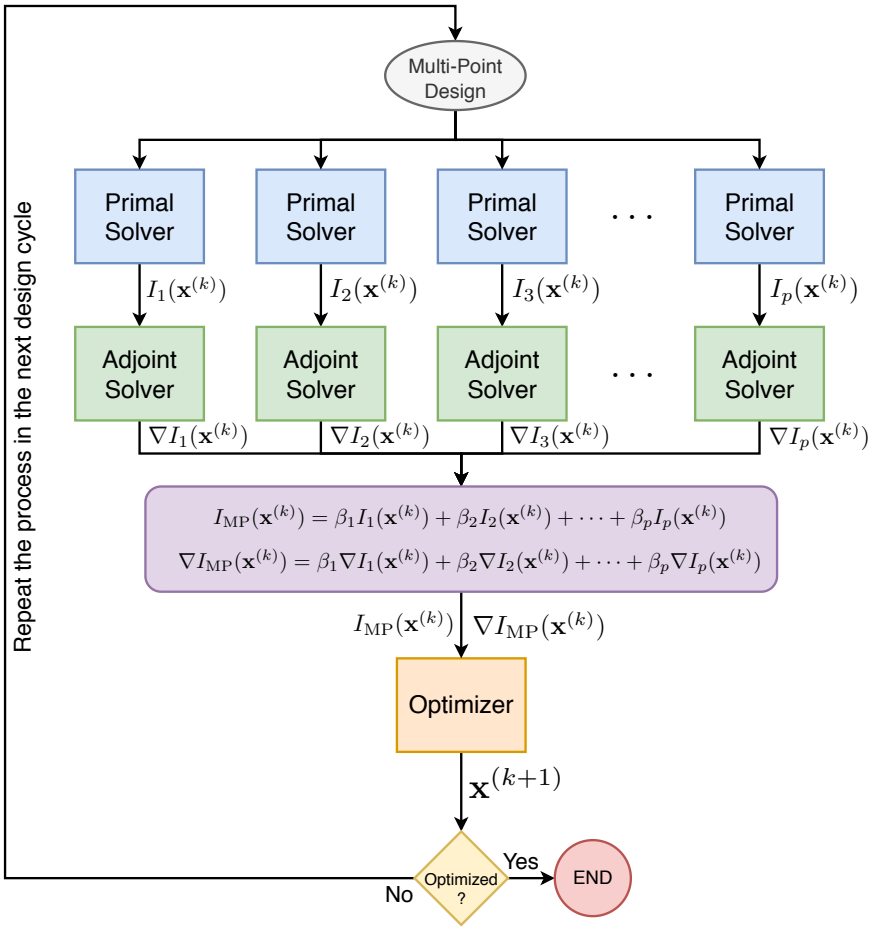

Figure 2. Flowchart of the multi-point design optimization process.

Table 1. Different operating conditions for the Caradonna-Tung[21] rotor in hover.

Case	θ_p (deg)	β_c (deg)	M_{tip}	Ω (RPM)
Non-Lifting	0.0	0.0	0.52	1482.3
Lifting	8.0	0.5	0.439	1250
Lifting	8.0	0.5	0.877	2500

direction. Riemann characteristic-based boundary conditions are applied at the far-field boundaries which are placed upstream and downstream of the rotor blade at a distance of 12 and 20 chord lengths away, respectively. A hybrid mesh with 370, 253 cells is generated which consists of 363, 961 tetrahedral and 6, 292 pyramid elements. The near-field and far-field views of the computational mesh are shown in Fig. 3 which also depicts different boundary conditions that are used for these simulations.

A. Non-Lifting Rotor

To verify the performance of the primal solver in simulating the flow about three-dimensional rotors, we first study a nonlifting case. The Caradonna-Tung rotor in hover with a nonlifting configuration is a good case for testing the performance of the flow solver in the absence of any downwash effects and the blade-vortex interactions. For this nonlifting case the collective pitch angle is set to zero degree and the tip Mach number reported by the experimental study[21] is 0.52, which corresponds to a rotational rate (or angular velocity) of $\Omega = 1482.3$ RPM.

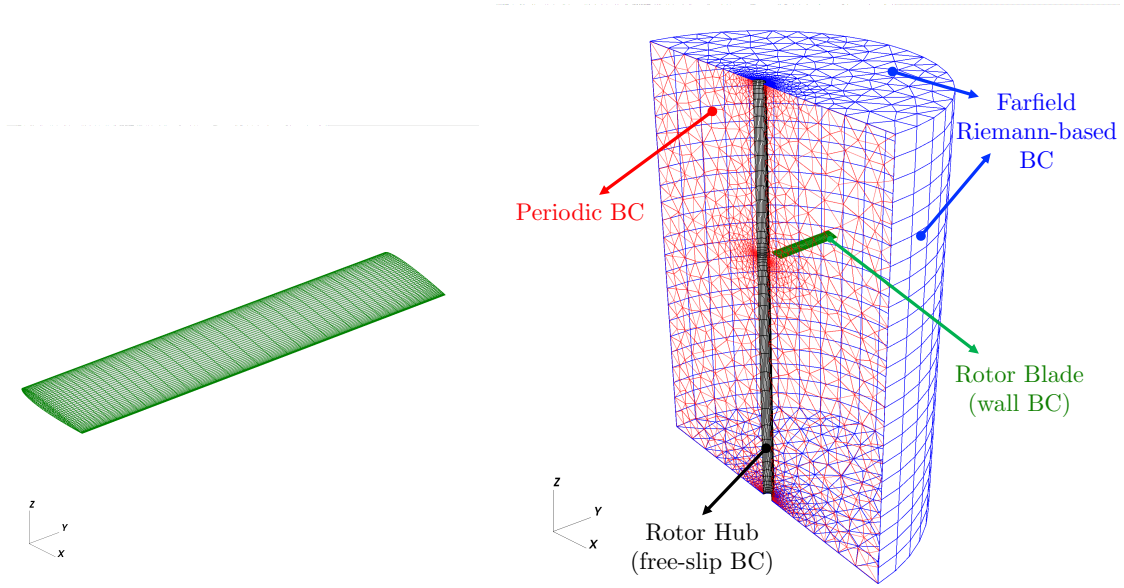

(a) Surface mesh of the rotor blade

(b) Computational domain and the boundary conditions

Figure 3. Near-field and far-field views of the computational domain depicting the surface and volume meshes for the Caradonna-Tung rotor cases.

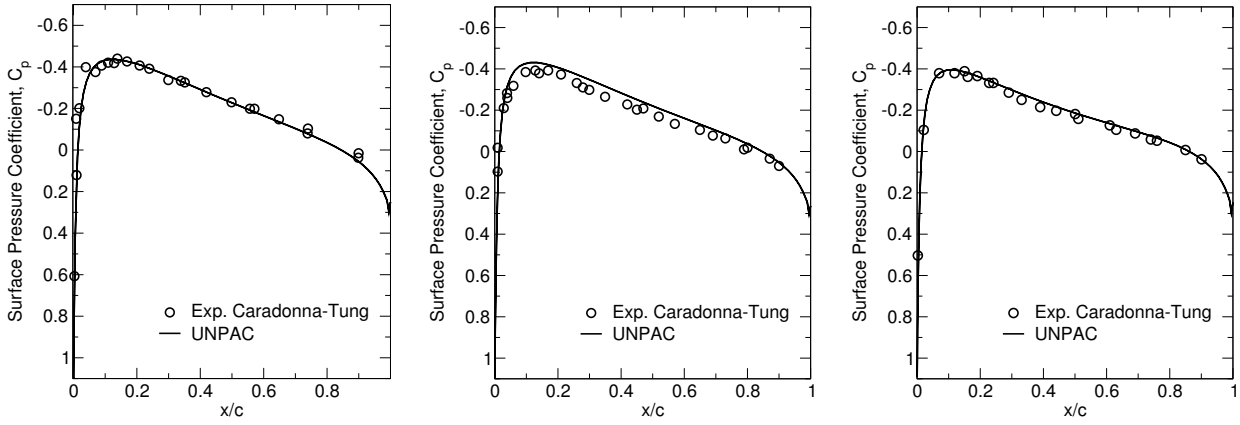

(a) 80% span

(b) 89% span

(c) 96% span

Figure 4. Coefficient of pressure distribution for the Caradonna-Tung rotor in hover (non-lifting conditions) with a tip Mach number of 0.52 and a collective pitch angle of $\theta_p = 0$ deg.

The C_p distributions at three spanwise locations, i.e., 80%, 89%, and 96% span, are shown in Fig. (4) for this nonlifting case. As can be seen, results at different span stations show an excellent agreement with the experimental data. Also, the flow is entirely subsonic along the rotor blade. Additionally, due to a symmetric cross-sectional geometry of the blades and a zero collective pitch angle, the pressure distributions are symmetric over the entire rotor blade surface.

B. Lifting Rotor with $M_{\text{tip}} = 0.439$

Next, we shift our attention to the lifting rotor cases with a collective pitch angle of 8 degrees. The first lifting case is based on a tip Mach number of 0.439 which corresponds to an angular velocity of 1250 RPM. Once again, the computed results are shown in Fig. (5) in terms of surface pressure coefficients defined as

$$C_p = \frac{p - p_\infty}{\frac{1}{2}\rho_\infty c_\infty^2 \left(M_{\text{tip}} \frac{r}{R_{\text{tip}}}\right)^2} \tag{18}$$

where p_∞, ρ_∞, and c_∞ are the pressure, density, and the speed of sound at the free-stream. Additionally, it can be seen that the dynamic pressure is defined as a function of the local rotational velocity.

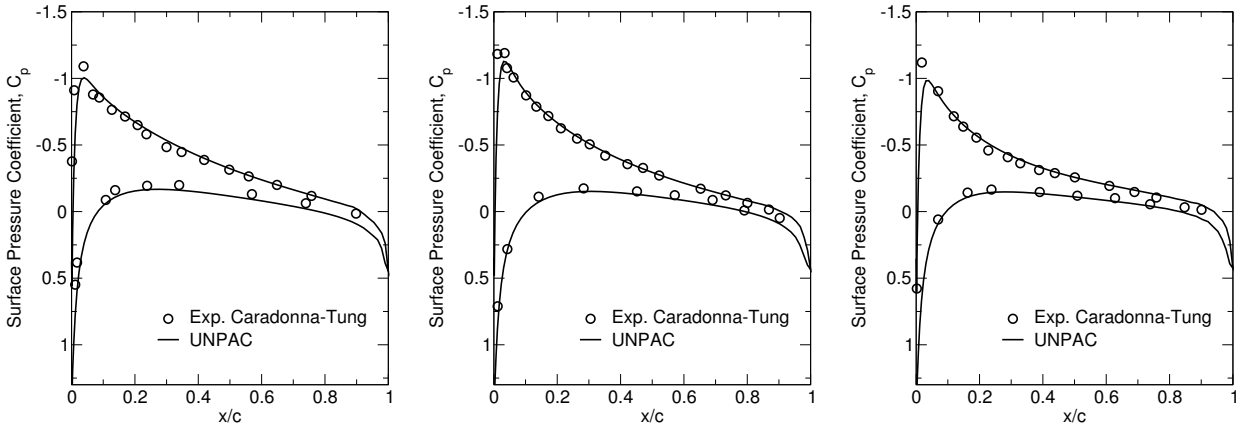

(a) 80% span (b) 89% span (c) 96% span

Figure 5. Coefficient of pressure distribution for the Caradonna-Tung rotor in hover (lifting conditions) at 1250 RPM (tip Mach number of 0.439) with the collective pitch angle of $\theta_p = 8$ deg.

Similar to the nonlifting case, the flow is once again subsonic along the blade for this particular case with a tip Mach number of 0.439. However, as can be seen in Fig. (5), the flow is no longer symmetric due to the collective pitch angle of the rotor and it also exhibits strong suction regions on the top surface of the rotor blades. Additionally, our results are in very good agreement with the experimental results of Caradonna and Tung.[21] It must be noted that for this case the rotor generates a thrust coefficient of $C_T = 0.004258$ and a torque coefficient of $C_Q = 0.000359$ with the figure of merit close to FM = 0.546256.

C. Lifting Rotor with $M_{\text{tip}} = 0.877$

As the last test case presented in this section, the flow around the Caradonna-Tung rotor in lifting hover conditions with a tip Mach number of 0.877 is considered. The collective pitch angle for this case is once again 8 degrees and the tip Mach number reported in the experimental study corresponds to an angular velocity of $\Omega = 2500$ RPM. In order to validate the numerical results obtained using the UNPAC solver, the surface pressure coefficients, C_p, at different spanwise locations are compared to the experimental data and the results are presented in Fig. (6).

For this high speed lifting case, the flow becomes transonic at about 70% span and the formation of the shock towards the tip of the blade can be clearly seen in Fig. (6). Once again, our results are in relatively good agreement with the experimental data at all spanwise locations. It must be noted that for this high rotational speed case, the rotor generates a thrust coefficient of $C_T = 0.004865$ and a torque coefficient of $C_Q = 0.000574$ which translates to a figure of merit of FM = 0.417538.

As a side note, the fully-automated in-house adjoint toolbox[38] takes about 30 minutes to obtain adjoint solutions while it takes almost 3 hours for the primal code to fully converge. Such an extremely efficient adjoint calculation at only a fraction of the computational cost of the primal solution enables us to perform large-scale single- and multi-point design optimization studies that will be presented next.

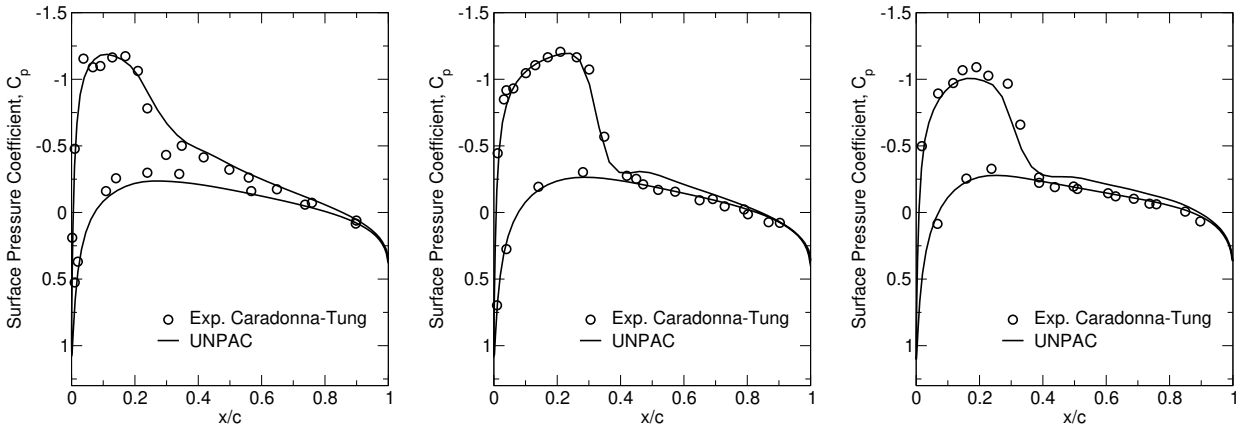

(a) 80% span (b) 89% span (c) 96% span

Figure 6. Coefficient of pressure distribution for the Caradonna-Tung rotor in hover (lifting conditions) at 2500 RPM (tip Mach number of 0.877) with the collective pitch angle of $\theta_p = 8$ deg.

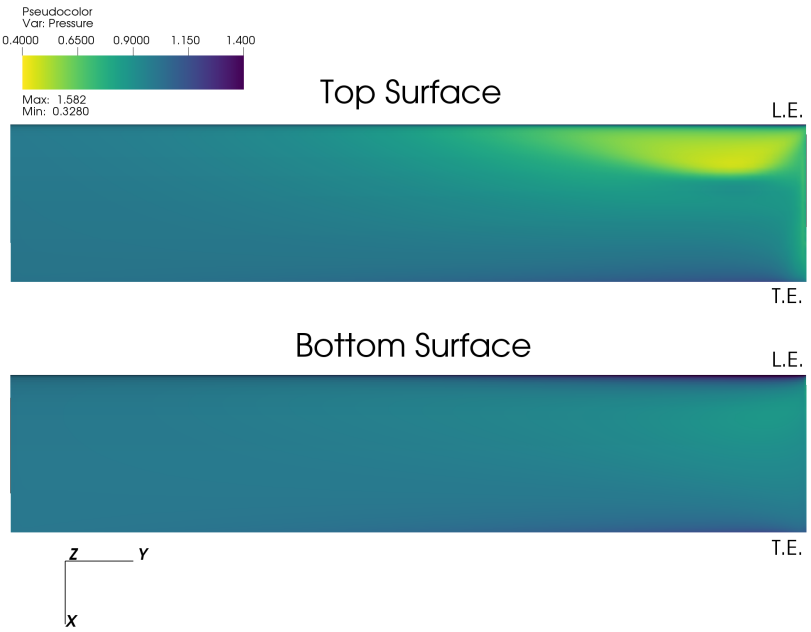

Figure 7. Pressure contours on the top and bottom surfaces of the Caradonna-Tung rotor in hover at 2500 RPM (tip Mach number of 0.877).

Additionally, the pressure contours on the top and bottom surfaces of a single rotor blade are shown in Fig. (7). Also, the adjoint solutions on the surface of the rotor blade are plotted to examine the sensitivities of the objective function, in this case the torque coefficient, for this high speed lifting case. These results are shown in Fig. (8) in terms of the density adjoints, $\overline{\rho}$, on the top and bottom surfaces of the Caradonna-Tung rotor. As can be seen, the most sensitive locations on the blade surface are in the vicinity of the shock and the expansion region upstream of the shock. It must be noted that similar behavior has been also reported by Economon et al.[54] using a continuous adjoint solver for this rotor case. Having presented the validation and verification results for the rotating frame of reference approach implemented in our in-house UNPAC solver, we now focus our attention to single- and multi-point design optimization results which will be discussed in the following section.

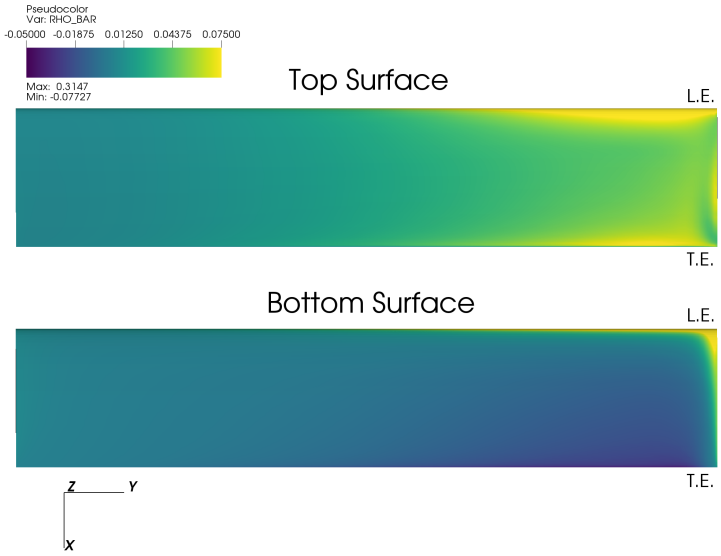

Figure 8. Adjoints of density, $\overline{\rho}$, on the top and bottom surfaces of the Caradonna-Tung rotor for the case with a tip Mach number of 0.877 and the collective pitch angle of 8 degrees. Here, the objective function is taken to be the torque coefficient, C_Q.

IV. Design Optimization Results

In this section, single- and multi-point design optimization of two- and three-dimensional configurations are sought. First, drag minimization is considered for a NACA0012 airfoil that rotates about an out-of-plane axis similar to a Vertical Axis Wind Turbine (VAWT) configuration. In this regard, single- and multi-point design optimizations that focus on minimizing the total drag coefficient are performed over a range of rotational speeds. Finally, the single- and multi-point design optimization of the Caradonna-Tung rotor is considered where the goal is to maximize the figure of merit by minimizing the torque of the rotor blade at various rotational speeds while maintaining a minimum thrust coefficient.

A. Drag Minimization of the Rotating NACA 0012 Airfoil

The first set of results presented in this work involves the unconstrained drag minimization of the NACA 0012 airfoil rotating about the out-of-page ($z-$) axis. The airfoil is rotated in still air with a zero free-stream Mach number. A similar test case was previously studied by Economon et al.[54] where a continuous adjoint Euler solver was used to optimize the geometry of the NACA 0012 airfoil. Here, the same reference temperature and pressure are used for the free-stream conditions while the rotational speed is varied between 75 RPM to 85 RPM in order to create three distinct design points (DP1 through DP3). These flow conditions are described in Table (2) for the primary (shown in **bold**) and secondary design points corresponding to different rotational speeds and their respective design weights.

Table 2. Different design points considered for the multi-point optimization of the rotating NACA 0012 airfoil.

Design Point	M_{tip}	ω_z (rad/s)	ω_z (RPM)	Design Weight, β
DP1	0.7575	7.85	75	1/4
DP2	**0.8080**	**8.38**	**80**	**1/2**
DP3	0.8585	8.90	85	1/4

Additionally, the center of rotation for this case is taken to be at point $(0.5c, -32c)$ with the airfoil having a unit chord length, i.e., $c = 1$. A two-dimensional Free-Form Deformation (FFD) box[35,38] is used to parameterize the airfoil geometry where the control points of the FFD box are taken to be the design variables. The goal of the optimization is to minimize the drag coefficient by deforming the geometry of the airfoil at three different rotational speeds corresponding to three separate design points as described in Table (2). This is initially done via standard single-point drag minimization focused on each design point. Following the single-point optimizations, the multi-point design optimization is performed where design point number 2 (primary design at 80 RPM) is given the highest weight, $\beta_2 = 0.5$, while the other two (secondary) design points each have a weight of 0.25. The unstructured mesh used for single- and multi-point design optimization problems is comprised of 10,216 triangular elements and 5,233 nodes.

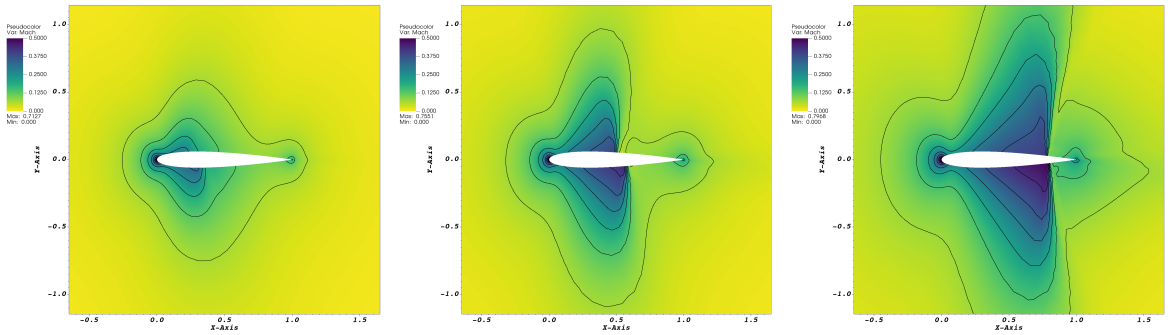

(a) DP1: 75 RPM (b) DP2: 80 RPM (c) DP3: 85 RPM

Figure 9. Absolute Mach number contour fields for the three design points considered for multi-point unconstrained drag minimization of the rotating NACA 0012 airfoil.

First, primal flow solutions in terms of the absolute Mach number contours are presented in Fig. (9). For the lowest rotational speed, the flow field remains mostly subsonic in the relative frame of reference. On the other hand, for the second and third design points, shocks and transonic flow regions appear on the pressure and suction sides of the airfoil which causes the relative local Mach number to exceed one in these regions. The shock strength is increased for the 85 RPM case and both shocks move further downstream and closer to the trailing edge of the airfoil.

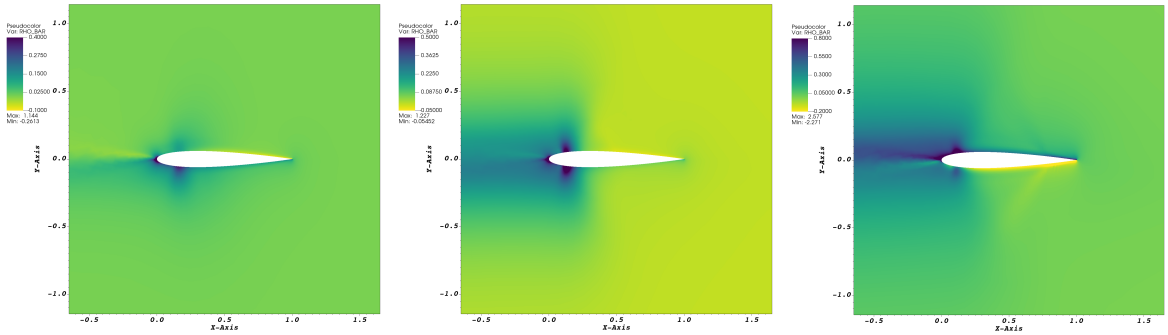

(a) DP1: 75 RPM (b) DP2: 80 RPM (c) DP3: 85 RPM

Figure 10. Adjoint of density, $\overline{\rho}$, contour fields obtained from the adjoint solvers for the three design points considered in the multi-point optimization of the rotating NACA 0012 airfoil.

Next, the adjoint of density contours obtained are presented in Fig. (10) for all three design points considered herein. For the adjoint sensitivity analysis, drag coefficient is used as the objective function which means that the density adjoints correspond to $\overline{\rho} = \partial C_D / \partial \rho$. As can be seen, the adjoint flow fields exhibit strong features close to the leading edge as well as the flow reversal which is typical of an adjoint

solution. Additionally, flow becomes more sensitive closer to the surface of the airfoil, especially for DP2 and DP3 cases that involve shocks on both sides of the airfoil. It is worth noting that the drag coefficient of the airfoil is significantly affected by the shock structure which explains the increased sensitivities of the drag count to flow solutions in the vicinity of the shock.

Table 3. Single-point unconstrained drag minimization results for the rotating NACA 0012 airfoil at three different design points.

	Design Point 1		Design Point 2		Design Point 3	
Design	C_D (count)	Reduction	C_D (count)	Reduction	C_D (count)	Reduction
Original	11.580	-	130.618	-	556.180	-
Optimal	-1.891	116.32%	10.206	92.18%	286.202	48.54%

Having presented the primal and adjoint flow fields, we now focus on the drag minimization problem. First, single-point optimizations are performed with the objective of minimizing the drag coefficient at each design point. As described earlier, the vertical movements of the FFD box control points are used as the design variables while fixing the leading and trailing edge points of the airfoil. Here, the L-BFGS-B optimizer is used for bound-constrained optimization where each design variable is kept within ±20% of its original value. These results are summarized in Table (3). As can be seen, it is possible to significantly reduce the drag coefficient of the airfoil in each design point. However, the drag coefficient at the first design point is reduced so much so that a negative value is obtained. This simply means that the single-point optimization is "ill-posed" for this design point.

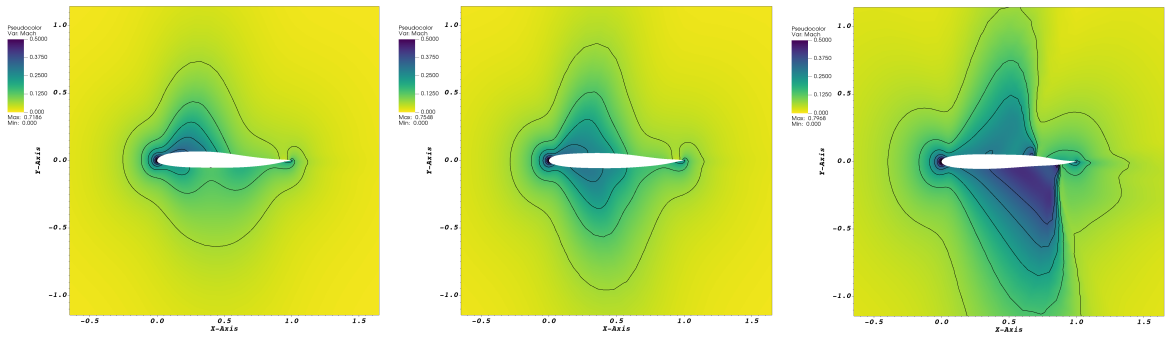

(a) DP1: 75 RPM (b) DP2: 80 RPM (c) DP3: 85 RPM

Figure 11. Absolute Mach number contour fields for the optimal designs obtained via single-point drag minimization of the rotating NACA 0012 airfoil.

Additionally, the absolute Mach number contours are presented in Fig. (11) for the optimal designs achieved via single-point drag minimization of the rotating NACA 0012 airfoil. More specifically, a direct comparison of the optimal solution for DP2 to the flow field obtained using the original design (Fig. [9]), reveals the elimination of the shock, which is the main contributing factor to the significant reduction of the drag coefficient for this design point. Furthermore, the strong shocks on the pressure and suction sides of the airfoil in DP3 are weakened resulting in a reduction in the drag coefficient for this design point as well. Due to the ill-posedness of the first design point, it is hard to explain the effects of the single-point drag minimization on the flow field. Nevertheless, it must be noted that the goal of minimizing the drag coefficient is still achieved for the single-point optimization of the airfoil rotating at 75 RPM.

Next, we present the multi-point design optimization results. As described earlier, the second design point at 80 RPM is considered the primary design point and is given a weight of $\beta_2 = 0.5$ while the other two design points have their weights set to $\beta_1 = \beta_3 = 0.25$. Once again, the vertical movements of the FFD box control points are used as the design variables with the control points at leading and trailing edges fixed in order to maintain a constant relative flow angle. Also, the same settings and bounds used for the single-point optimization are utilized for the L-BFGS-B optimizer. The multi-point drag minimization

results are presented in Table (4), which shows considerable reductions in the drag coefficients for all three design points.

Table 4. Multi-point unconstrained drag minimization results for the rotating NACA 0012 airfoil at three different design points.

	Design Point 1		Design Point 2		Design Point 3	
Design	C_D (count)	Reduction	C_D (count)	Reduction	C_D (count)	Reduction
Original	11.580	-	130.618	-	556.180	-
Optimal	7.459	35.58%	18.677	85.70%	322.485	42.01%

The first thing that can be noticed when studying the drag minimization results presented in Table (4) is the fact that the largest reduction in the drag coefficient is achieved for the second design point. This behavior was expected considering the fact that the second design point was chosen as the primary point with a higher weight. Additionally, the first design point is no longer "ill-posed" which means that the multi-point optimization approach leads to better designs for a wider range of rotational speeds.

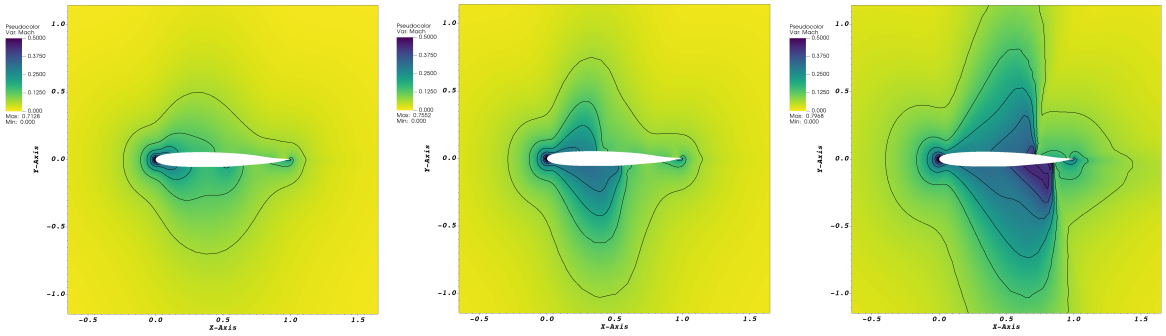

(a) DP1: 75 RPM (b) DP2: 80 RPM (c) DP3: 85 RPM

Figure 12. Absolute Mach number contour fields for the "unique" optimal design obtained via the proposed multi-point design optimization approach (rotating NACA 0012 airfoil).

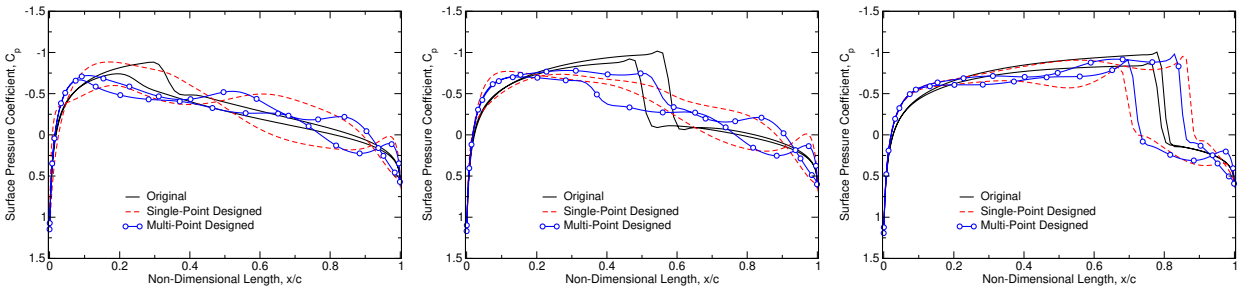

(a) DP1: 75 RPM (b) DP2: 80 RPM (c) DP3: 85 RPM

Figure 13. Comparison of the surface pressure distributions for the original, single-point, and multi-point designs of the rotating NACA 0012 airfoil.

Next, the absolute Mach number contours are presented in Fig. (12) for the optimal design achieved via a multi-point drag minimization approach for the rotating NACA 0012 airfoil. As can be seen, similar flow features can be noticed in these contour fields compared to those achieved from a single-point design approach (see Fig. [11]). However, in the case of the multi-point design, a unique shape is obtained for

the optimal airfoil that can provide improvements in a wide range of flow regimes corresponding to various rotational speeds.

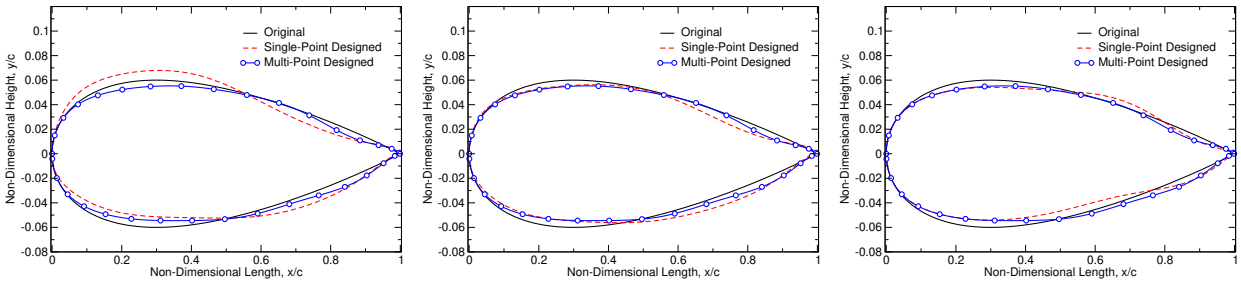

(a) DP1: 75 RPM (b) DP2: 80 RPM (c) DP3: 85 RPM

Figure 14. Comparison of the airfoil geometries for the original, single-point, and multi-point designs of the rotating NACA 0012 airfoil.

Finally, surface pressure distributions as well as the airfoil geometries are compared for the original, single-point, and multi-point designs studied in this work. The surface pressure coefficients are presented in Fig. (13) while original and deformed airfoil geometries are shown in Fig. (14). Once again, for DP2, both shocks on the two sides of the original airfoil have been eliminated. Additionally, the strong shocks for DP3 are weakened while a more uniform surface distribution is achieved for the design point at the lowest rotational speed (DP1). Moreover, the multi-point design optimization has led to a more smooth airfoil geometry compared to the more extreme deformations that were seen for the single-point optimization of DP1 and DP3. This smooth deformation once again proves that the proposed multi-point optimization approach is well-posed.

B. Thrust-Constrained Torque Minimization of the Caradonna-Tung Rotor

In this section, single- and multi-point design optimization results for the Caradonna-Tung rotor are presented. As previously discussed, the main objective of this design optimization is to minimize the torque coefficient while maintaining a minimum thrust coefficient as described in Eq. (13). Here, two design points are considered which are both in hover conditions and at relatively high rotational speeds. The two design points are described in Table (5) which also includes the weights for the multi-point optimization approach. As can be seen, two different multi-point design cases are considered, named MPD1 and MPD2, where weights assigned to each design point are varied. Additionally, in order to compare the multi-point design optimization results with conventional design approach, the rotor is also designed using a single-point design (SPD) approach at 2250 RPM and 2500 RPM.

Table 5. Two different design points (DP1 and DP2) studied for the single- and multi-point design of the Caradonna-Tung rotor.

Design Point	RPM	M_{tip}	MPD1, β	MPD2, β
DP1	2250	0.794	1/2	1/3
DP2	2500	0.877	1/2	2/3

It must be noted that the minimum thrust coefficient that is set for both design points is $C_{T\min} = 0.0046$ which translates to a 5% reduction in the thrust generated by the original rotor design. Since sensitivities of the objective function are greatest close to the tip of the rotor, the FFD box is designed such that it only covers the tip region (beyond 60% spanwise location) to focus more on shape deformations in this region. The FFD box used in the single- and multi-point design cases is shown in Fig. (15) where 11 points are used in both chordwise and spanwise directions. The control points of the FFD box are allowed to move at the leading and trailing edge while a symmetric movement is enforced to avoid any extreme shape deformation.

It is worth noting that the z-components of the FFD box control points are used as the design variables for the optimization problem presented in this section with a total of 200 design variables.

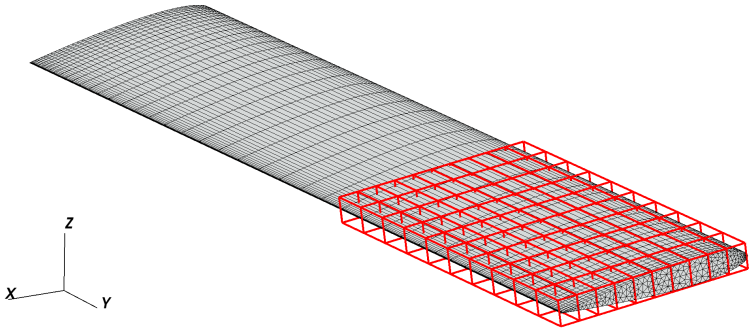

Figure 15. Free Form Deformation (FFD) box used for shape parameterization of the Caradonna-Tung rotor.

The first set of results presented are the surface pressure contours for the two design points, i.e., at 2250 and 2500 RPM, considered herein. These results are shown in Figs. (16) through (19) for the single- and multi-point design optimization cases. As shown previously in Section III, the lifting case at 2500 RPM in hover results in transonic shocks forming on the top surface of the rotor starting from the 80% spanwise location. It is interesting to note that the single-point design optimization of this high speed case (at 2500 RPM) leads to a design with weaker shocks which results in significant reductions of the torque coefficient.

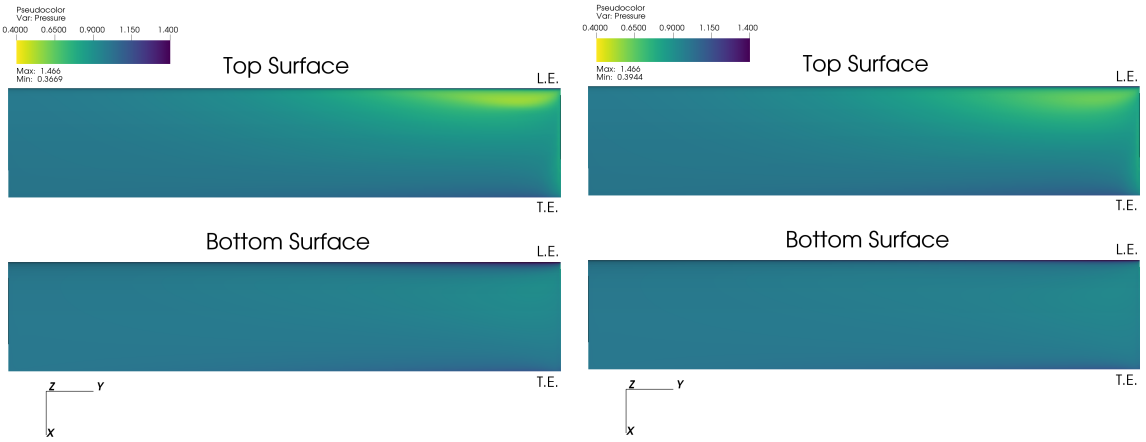

(a) Original Design

(b) Single-Point Design

Figure 16. Pressure contours on the top and bottom surfaces of the Caradonna-Tung rotor for the original and single-point design (SPD) cases (hover at 2250 RPM).

Similar results are also achieved for the lower rotational speed case. However, the reductions in torque coefficient are less significant for the DP1 case (at 2250 RPM) due to the weaker shocks for this case in the original design. On the other hand, as shown in previous section for the rotating NACA 0012 airfoil, the multi-point design approach more often leads to less significant reductions in the quantity of interest while leading to a design that has better aerodynamic characteristics at various design points. This phenomenon can be clearly seen in Figs. (18) and (19) where changes in the surface pressure compared to the original design are very small. However, even the small changes in the design of the rotor blade have led to better performance at both design points.

In order to better compare the single- and multi-point design optimization results, original and optimal quantities of interest are studied in terms of thrust coefficient, torque coefficient, figure of merit, and the thrust-to-torque ratio and the values are presented in Table (6). Clearly, the single-point design of the rotor leads to the best performance gain at both design points. However, it is important to note that the

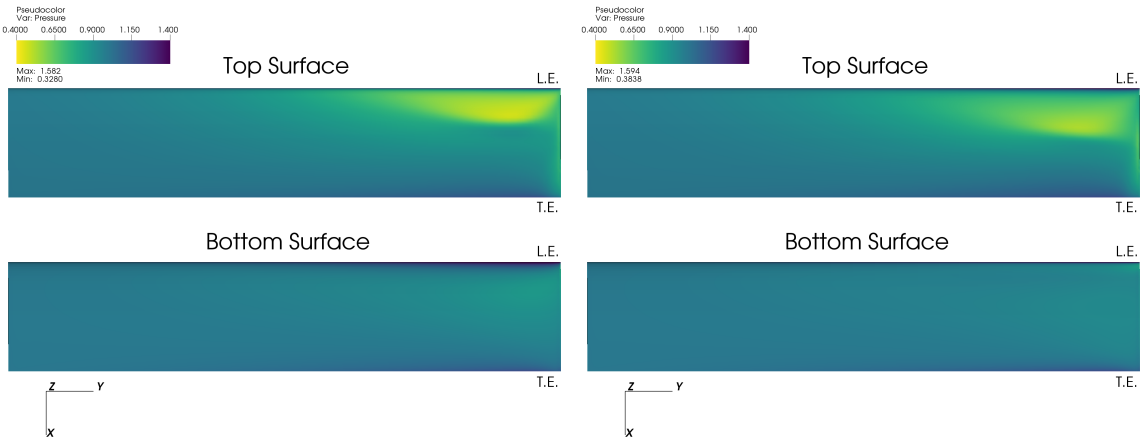

(a) Original Design (b) Single-Point Design

Figure 17. Pressure contours on the top and bottom surfaces of the Caradonna-Tung rotor for the original and single-point design (SPD) cases (hover at 2500 RPM).

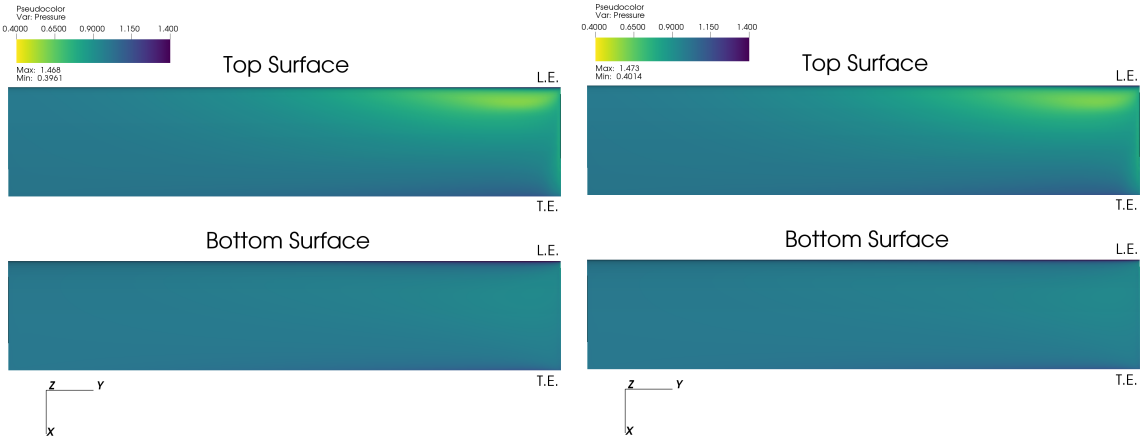

(a) Multi-Point Design 1 (b) Multi-Point Design 2

Figure 18. Pressure contours on the top and bottom surfaces of the Caradonna-Tung rotor for the two different multi-point design (MPD1 and MPD2) cases (hover at 2250 RPM).

multi-point design of the rotor is also capable of providing considerable improvements in the aerodynamic performance. Additionally, the second multi-point design case, which gives a higher weight to the higher rotational speed design point, i.e., 2500 RPM, ultimately leads to a better optimal result. This was expected since the 2500 RPM design point exhibits strong transonic shock and achieving weaker shocks at this design point would potentially mean lower torque coefficient at other transonic design points.

Next, the deformations of the FFD box are presented for the single- and multi-point design cases in Figs. (20) and (21). As can be seen, displacement of the FFD box control points at the leading edge of the rotor is more pronounced. Also, the second design point at the higher rotational speed once again exhibits more extreme shape deformations due to its strong shock formation as well as the expansion region upstream of the shock and close to the tip of the rotor.

While surface pressure contours presented earlier show the weakening of the shocks around the tip regions, we now focus on the pressure coefficient distributions at three spanwise locations for the single- and multi-point design cases. These results are shown in Figs. (22) and (23) for the two design points. Once again, it

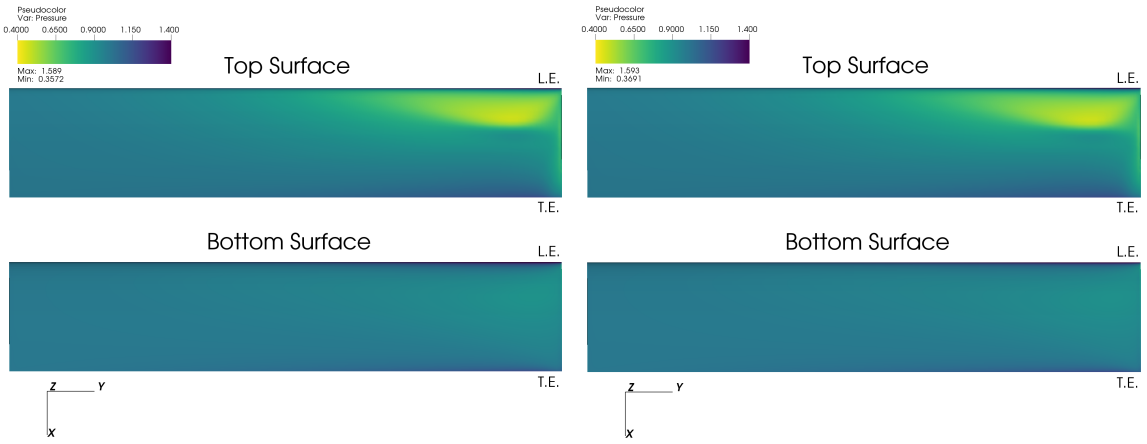

(a) Multi-Point Design 1

(b) Multi-Point Design 2

Figure 19. Pressure contours on the top and bottom surfaces of the Caradonna-Tung rotor for the two different multi-point design (MPD1 and MPD2) cases (hover at 2500 RPM).

Table 6. Results from the single-point and multi-point designs of the Caradonna-Tung rotor at two different rotational speeds in hover.

Design Point	C_T	change	C_Q	change	FM	change	C_T/C_Q	change
DP1-Original	0.004825	-	0.0005129	-	0.462121	-	9.407837	-
DP1-SPD	0.004589	**-4.89%**	0.0004623	**-9.86%**	0.475576	**+2.91%**	9.927527	**+5.52%**
DP1-MPD1	0.004603	**-4.60%**	0.0004687	**-8.61%**	0.471164	**+1.95%**	9.820966	**+4.39%**
DP1-MPD2	0.004558	**-5.53%**	0.0004584	**-10.62%**	0.474736	**+2.72%**	9.943439	**+5.69%**
DP2-Original	0.004865	-	0.0005747	-	0.417538	-	8.465456	-
DP2-SPD	0.004594	**-5.57%**	0.0005023	**-12.59%**	0.438332	**+4.98%**	9.145522	**+8.03%**
DP2-MPD1	0.004646	**-4.50%**	0.0005306	**-7.67%**	0.4220920	**+1.09%**	8.756814	**+3.44%**
DP2-MPD2	0.004605	**-5.34%**	0.0005203	**-9.46%**	0.4247437	**+1.72%**	8.851330	**+4.55%**

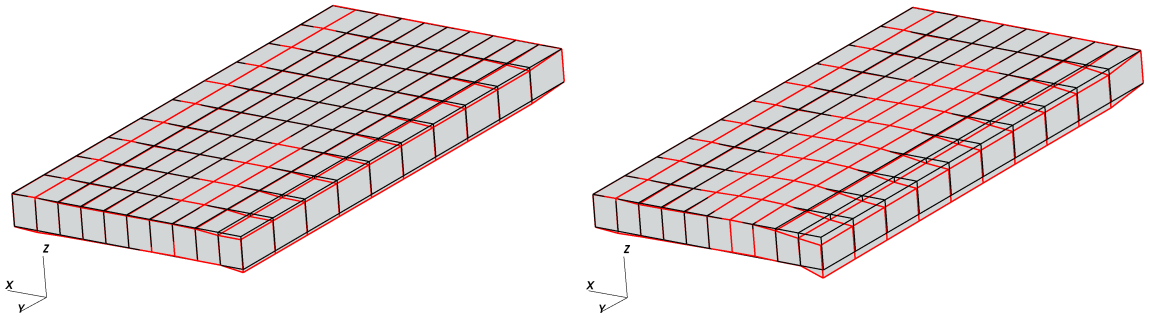

(a) SPD: 2250 RPM

(b) SPD: 2500 RPM

Figure 20. Deformation of the FFD box for the single-point design of the Caradonna-Tung rotor at two different rotational speeds at hover.

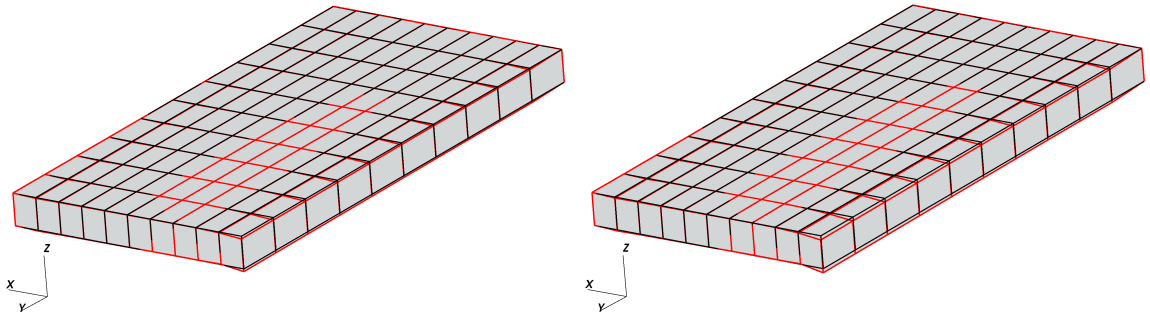

(a) Multi-Point Design 1 (b) Multi-Point Design 2

Figure 21. Deformation of the FFD box for the multi-point designs (MPD1 and MPD2) of the Caradonna-Tung rotor at two different rotational speeds at hover.

can be seen that the most extreme changes in the surface pressure distributions are experienced for the single-point design at 2500 RPM. Additionally, the cross-sectional geometries of the rotor at the same spanwise locations are compared for all the design cases studied here and the results are shown in Figs. (24) and (25).

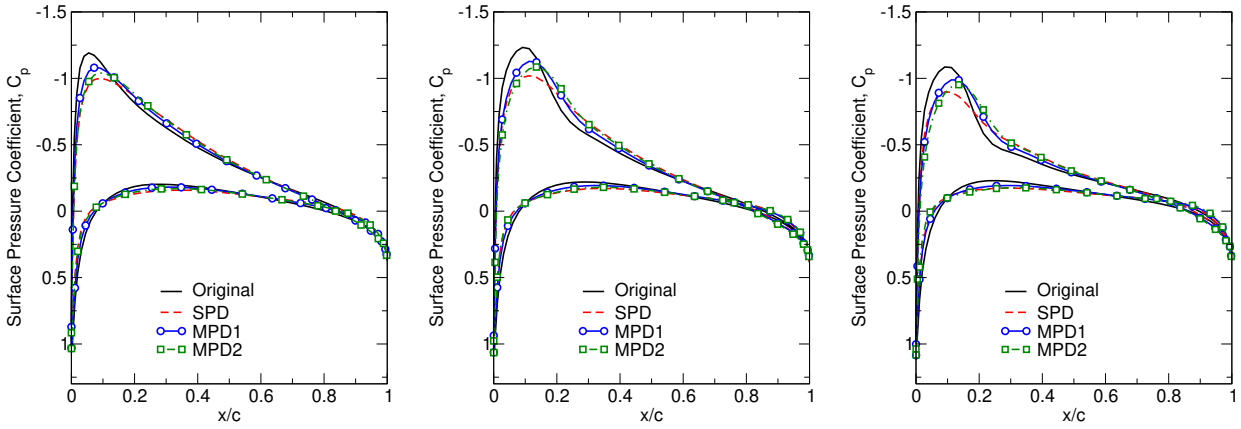

(a) 80% span (b) 89% span (c) 96% span

Figure 22. Coefficient of pressure distribution for the Caradonna-Tung rotor in hover at 2250 RPM for the original, single-point, and multi-point designs.

The convergence histories of different quantities of interest for the single- and multi-point design optimization cases studied are presented next. Note that all quantities are normalized with respect to their original value and these relative values are plotted in terms of thrust and torque coefficients, figure of merit, and thrust-to-torque ratio. These results are presented in Figs. (26) through (29) for the single- and multi-point design cases. The minimum thrust coefficient used in the penalty function approach for the thrust-constrained torque minimization problem is also marked on these plots. Significant reductions in the torque coefficient are achieved while a minimum thrust coefficient is maintained. Therefore, the figure of merit as well as the thrust-to-torque ratio are increased which means that the aerodynamic characteristics and performance of the Caradonna-Tung rotor are improved.

Finally, the optimal design from the two multi-point optimizations are used to test their performance at a much lower rotational speed in order to study the performance of a multi-point design on an "off-design" condition. For this reason, the hover condition at 1750 RPM is considered with the same pitch angle of 8 degrees. The numerical results are presented in terms of surface pressure contours on the surface of the rotor. These contours are shown in Fig. (30) for the original design as well as the two multi-point design

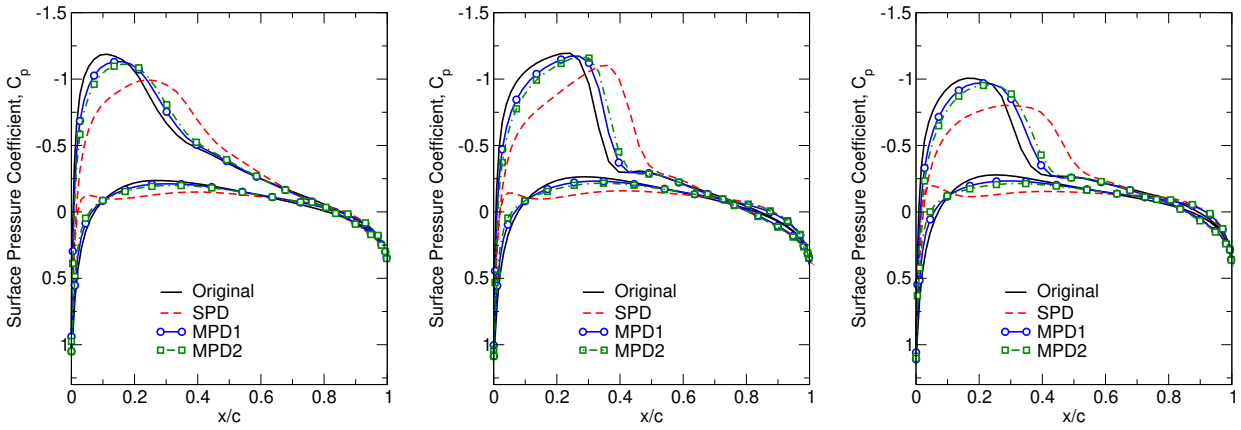

(a) 80% span (b) 89% span (c) 96% span

Figure 23. Coefficient of pressure distribution for the Caradonna-Tung rotor in hover at 2500 RPM for the original, single-point, and multi-point designs.

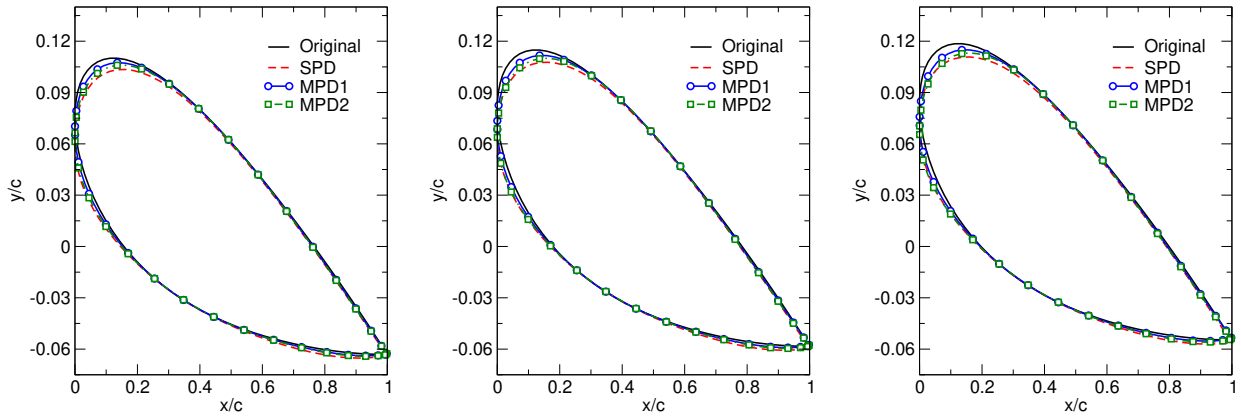

(a) 80% span (b) 89% span (c) 96% span

Figure 24. Cross-sectional geometries of the Caradonna-Tung rotor in hover at 2250 RPM for the original, single-point, and multi-point designs.

cases studied earlier.

Table 7. Results from the off-design case of the Caradonna-Tung rotor running at 1750 RPM using the original as well as the multi-point-designed geometries.

Design	C_T	change	C_Q	change	FM	change	C_T/C_Q	change
Original	0.005006	-	0.0004923	-	0.508650	-	10.16859	-
MPD1	0.004760	**-4.91%**	0.0004467	**-9.26%**	0.519893	**+2.21%**	10.65592	**+4.79%**
MPD2	0.004722	**-5.67%**	0.0004384	**-10.94%**	0.523400	**+2.89%**	10.77098	**+5.92%**

Additionally, the aerodynamic characteristics of the rotor running at 1750 RPM are presented in Table (7) for the original and MPD1/MPD2 optimal designs. As can be seen, the figure of merit as well as the thrust-to-torque ratio are both increased for this off-design case at 1750 RPM while the optimal geometry used here was achieved by performing multi-point designs using 2250 and 2500 RPM rotational speeds. This

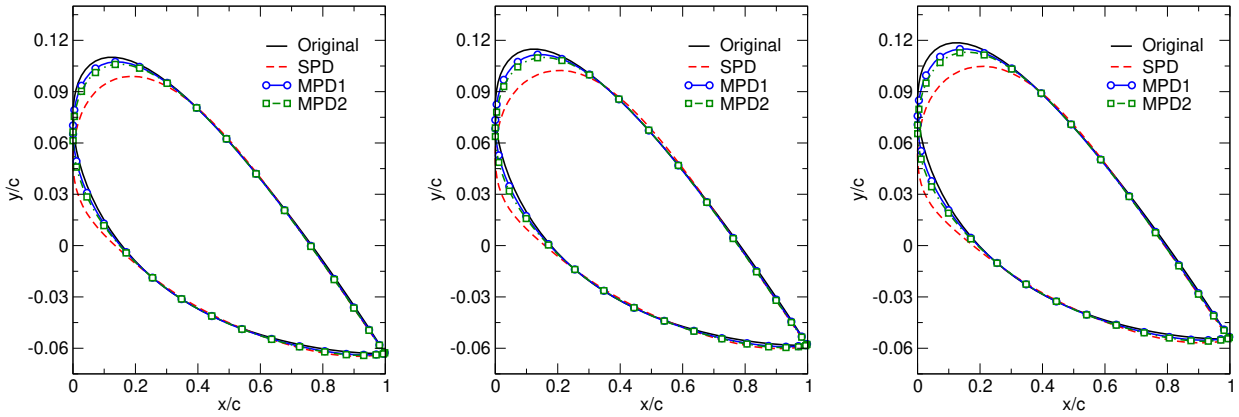

(a) 80% span (b) 89% span (c) 96% span

Figure 25. Cross-sectional geometries of the Caradonna-Tung rotor in hover at 2500 RPM for the original, single-point, and multi-point designs.

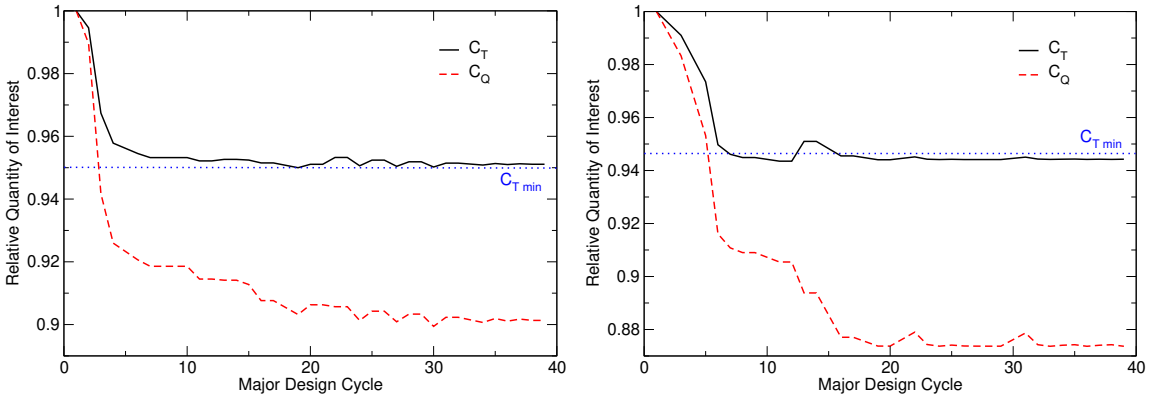

(a) SPD: 2250 RPM (b) SPD: 2500 RPM

Figure 26. Convergence of the thrust and torque coefficients for the single-point design of the Caradonna-Tung rotor in hover at 2250 and 2500 RPM.

is an interesting result since it clearly shows the potential of the proposed multi-point design approach in providing improvements for a wider range of design points.

V. Conclusions

An aerodynamic design optimization framework based on a memory efficient discrete-adjoint toolbox was developed for single- and multi-point design of helicopter rotor blades in hover. The discrete adjoint sensitivity analysis was carried out using an in-house fully-automated toolbox called FDOT. Additionally, an in-house CFD solver (called UNPAC) that can model flows in a rotating frame of reference was used to efficiently compute flows around helicopter rotor blades. The developed framework was first used to simulate flow around the Caradonna and Tung rotor in hover with non-lifting and lifting configurations for validation. Next, the aerodynamic design optimization framework was used for drag minimization for a rotating NACA 0012 airfoil. Both single- and multi-point design approaches were considered. The multi-point optimization lead to a well-posed design space, and an "optimal" design was attained for improved aerodynamic characteristics over a wide range of flow regimes and rotational speeds. Ultimately, the Caradonna and Tung

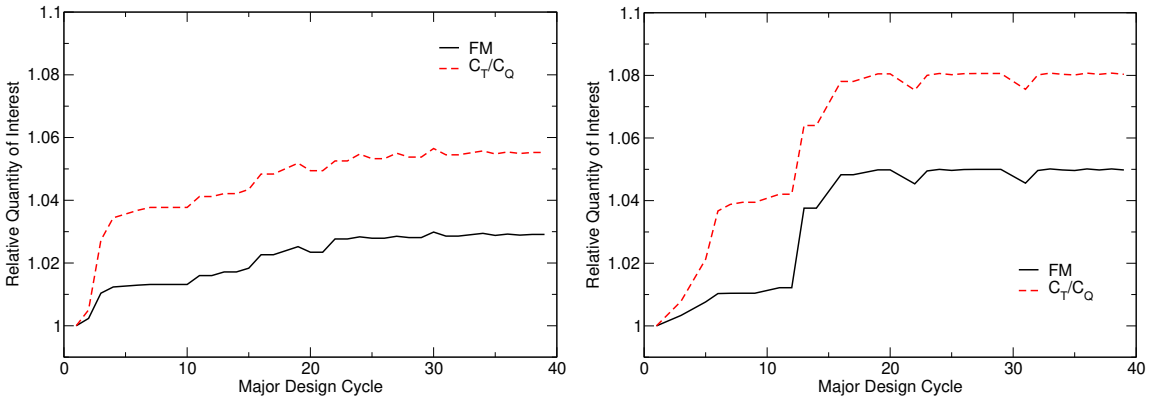

(a) SPD: 2250 RPM

(b) SPD: 2500 RPM

Figure 27. Convergence of the figure of merit and the thrust-to-torque ratio for the single-point design of the Caradonna-Tung rotor in hover at 2250 and 2500 RPM.

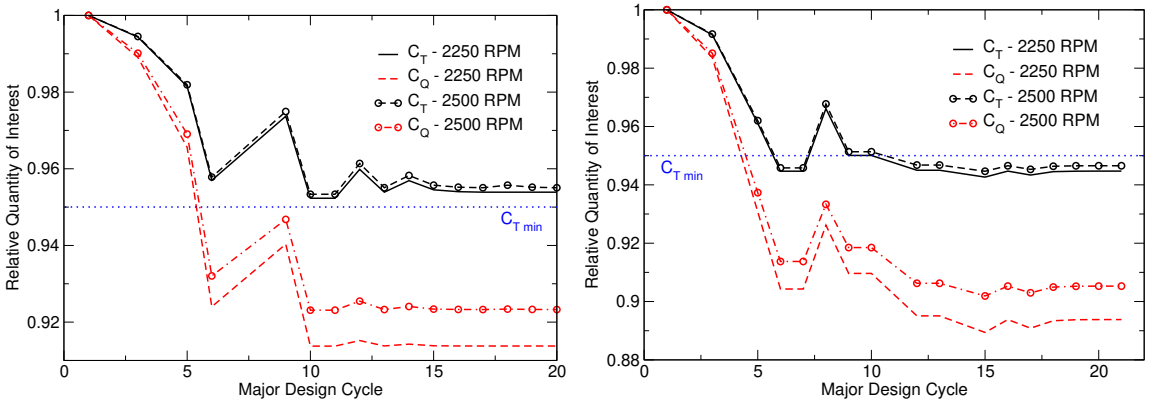

(a) Multi-Point Design 1

(b) Multi-Point Design 2

Figure 28. Convergence of the thrust and torque coefficients for the two multi-point design cases of the Caradonna-Tung rotor in hover.

rotor design was "fine-tuned" to improve the figure of merit over a range of rotational speeds. In this regard, a thrust-constrained torque minimization approach was considered using both single- and multi-point optimization approaches. Numerical results showed a clear improvement in the figure of merit as well as the thrust-to-torque ratio for various rotational speeds. Finally, it must be noted that the proposed multi-point optimization framework based on the FDOT toolbox can be directly coupled – in a "black-box" manner – with other existing codes in Helios, which is part of the CREATE-AV platform.

VI. Acknowledgments

This material is based upon work supported by the National Science Foundation under grant No: CBET-1803760. The authors greatly appreciate the support provided.

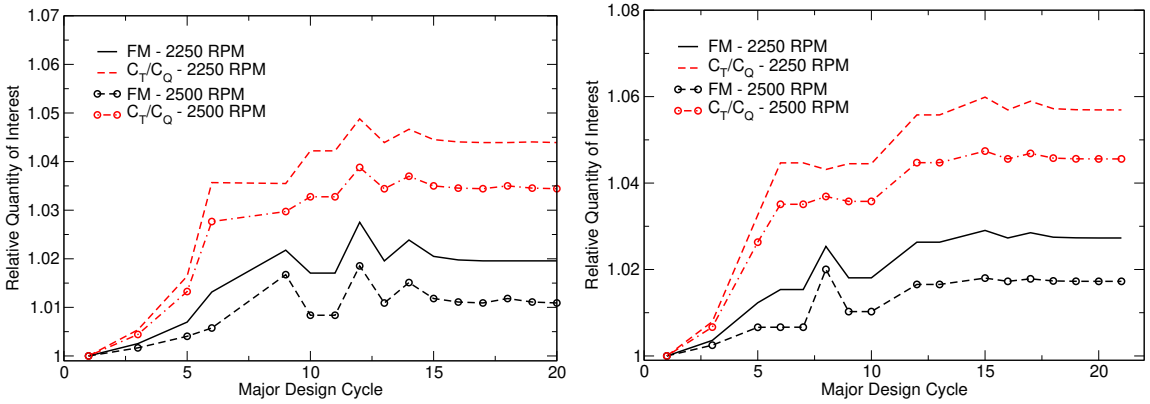

(a) Multi-Point Design 1

(b) Multi-Point Design 2

Figure 29. Convergence of the figure of merit and the thrust-to-torque ratio for the two multi-point design cases of the Caradonna-Tung rotor in hover.

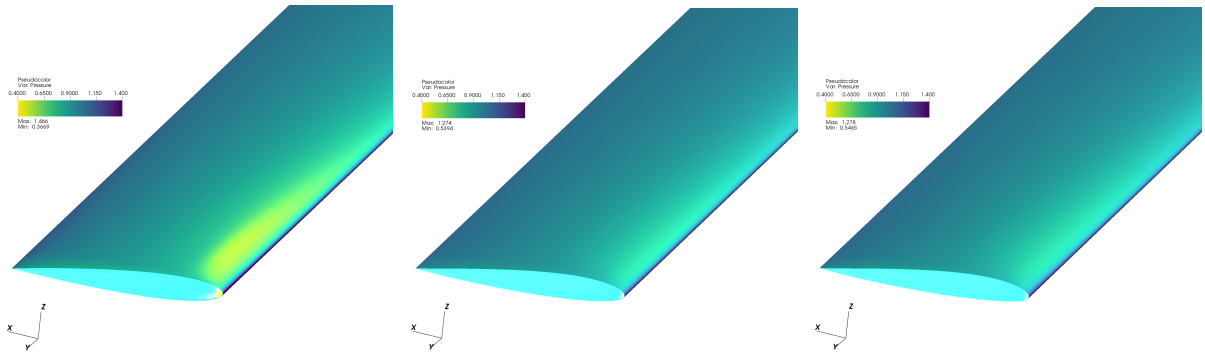

(a) Original Design

(b) Multi-Point Design 1

(c) Multi-Point Design 2

Figure 30. Pressure contours on the surface of the Caradonna-Tung rotor for the off-design case (at 1750 RPM) using the original and the two multi-point design geometries.

References

[1]Caradonna, F. X. and Isom, M. P., "Subsonic and transonic potential flow over helicopter rotor blades," *AIAA Journal*, Vol. 10, No. 12, 1972, pp. 1606–1612.

[2]Caradonna, F. X. and Isom, M. P., "Numerical calculation of unsteady transonic potential flow over helicopter rotor blades," *AIAA Journal*, Vol. 14, No. 4, 1976, pp. 482–488.

[3]Agarwal, R. and Deese, J., "Euler calculations for flowfield of a helicopter rotor in hover," *Journal of Aircraft*, Vol. 24, No. 4, 1987, pp. 231–238.

[4]SrinivaSan, G. R., Baeder, J., Obayashi, S., and McCroskey, W., "Flowfield of a lifting rotor in hover - A Navier-Stokes simulation," *AIAA journal*, Vol. 30, No. 10, 1992, pp. 2371–2378.

[5]Pomin, H. and Wagner, S., "Navier-Stokes analysis of helicopter rotor aerodynamics in hover and forward flight," *Journal of Aircraft*, Vol. 39, No. 5, 2002, pp. 813–821.

[6]Allen, C., "Numerical Simulation of Multi-Bladed Rotors in Lifting Forward Flight," AIAA Paper 2003-4080, 2003.

[7]Ekici, K., Hall, K. C., and Dowell, E. H., "Computationally fast harmonic balance methods for unsteady aerodynamic predictions of helicopter rotors," *Journal of Computational Physics*, Vol. 227, No. 12, 2008, pp. 6206–6225.

[8]Butsuntorn, N. and Jameson, A., "Time spectral method for rotorcraft flow," AIAA Paper 2008-403, 2008.

[9]Tatossian, C. A., Nadarajah, S. K., and Castonguay, P., "Aerodynamic shape optimization of hovering rotor blades using a Non-Linear Frequency Domain approach," *Computers & fluids*, Vol. 51, No. 1, 2011, pp. 1–15.

[10]Choi, S., Alonso, J., Weide, E., and Sitaraman, J., "Validation study of aerodynamic analysis tools for design optimization of helicopter rotors," AIAA Paper 2007-3929, 2007.

[11]Choi, S., Lee, K. H., Alonso, J. J., and Datta, A., "Preliminary Study on Time-Spectral and Adjoint-Based Design Optimization of Helicopter Rotors," *AHS specialist meeting, San Francisco, CA*, 2008.

[12]Choi, S., Lee, K., Potsdam, M. M., and Alonso, J. J., "Helicopter rotor design using a time-spectral and adjoint-based method," *Journal of Aircraft*, Vol. 51, No. 2, 2014, pp. 412–423.

[13]Le Pape, A. and Beaumier, P., "Numerical optimization of helicopter rotor aerodynamic performance in hover," *Aerospace science and technology*, Vol. 9, No. 3, 2005, pp. 191–201.

[14]Vu, N. A., Lee, J. W., and Shu, J. I., "Aerodynamic design optimization of helicopter rotor blades including airfoil shape for hover performance," *Chinese Journal of Aeronautics*, Vol. 26, No. 1, 2013, pp. 1–8.

[15]Morris, A., Allen, C., and Rendall, T., "Development of generic CFD-based aerodynamic optimisation tools for helicopter rotor blades," AIAA Paper 2007-3809, 2007.

[16]Pironneau, O., "On optimum design in fluid mechanics," *Journal of Fluid Mechanics*, Vol. 64, No. 01, 1974, pp. 97–110.

[17]Jameson, A., "Aerodynamic design via control theory," *Journal of Scientific Computing*, Vol. 3, No. 3, 1988, pp. 233–260.

[18]Anderson, W. K. and Venkatakrishnan, V., "Aerodynamic design optimization on unstructured grids with a continuous adjoint formulation," *Computers & Fluids*, Vol. 28, No. 4, 1999, pp. 443–480.

[19]Kirn, S., Alonso, J. J., and Jameson, A., "Design optimization of high-lift configurations using a viscous continuous adjoint method," AIAA Paper 2002-0844, 2002.

[20]Lee, S. W. and Kwon, O. J., "Aerodynamic shape optimization of hovering rotor blades in transonic flow using unstructured meshes," *AIAA journal*, Vol. 44, No. 8, 2006, pp. 1816–1825.

[21]Caradonna, F. X. and Tung, C., "Experimental and analytical studies of a model helicopter rotor in hover," *NASA/TM 81232, NASA Ames Research Center, Moffett Field, CA*, 1981.

[22]Nadarajah, S. and Jameson, A., "A comparison of the continuous and discrete adjoint approach to automatic aerodynamic optimization," AIAA Paper 2000-0667, 2000.

[23]Giles, M. B., Duta, M. C., Müller, J.-D., and Pierce, N. A., "Algorithm developments for discrete adjoint methods," *AIAA Journal*, Vol. 41, No. 2, 2003, pp. 198–205.

[24]Djeddi, S., *Towards Adaptive and Grid-Transparent Adjoint-Based Design Optimization Frameworks*, Ph.D. thesis, University of Tennessee, 2018.

[25]Rivers, M. B. and Dittberner, A., "Experimental investigations of the NASA common research model," *Journal of Aircraft*, Vol. 51, No. 4, 2014, pp. 1183–1193.

[26]Kenway, G. K. and Martins, J. R., "Multipoint aerodynamic shape optimization investigations of the Common Research Model wing," *AIAA Journal*, Vol. 54, No. 1, 2016, pp. 113–128.

[27]Wang, J. F. and Periaux, J., "Multi-point optimization using gas and Nash/Stackelberg games for high lift multi-airfoil design in aerodynamics," *Proceedings of the 2001 Congress on Evolutionary Computation (IEEE Cat. No. 01TH8546)*, Vol. 1, IEEE, 2001, pp. 552–559.

[28]Toal, D. J. and Keane, A. J., "Efficient multipoint aerodynamic design optimization via cokriging," *Journal of Aircraft*, Vol. 48, No. 5, 2011, pp. 1685–1695.

[29]Leoviriyakit, K. and Jameson, A., "Multipoint wing planform optimization via control theory," AIAA Paper 2005-450, 2005.

[30]Jameson, A., Leoviriyakit, K., and Shankaran, S., "Multi-point aero-structural optimization of wings including planform variations," AIAA Paper 2007-764, 2007.

[31]Demeulenaere, A., Ligout, A., and Hirsch, C., "Application of multipoint optimization to the design of turbomachinery blades," *ASME Turbo Expo 2004: Power for Land, Sea, and Air*, American Society of Mechanical Engineers Digital Collection, 2004, pp. 1481–1489.

[32]Arabnia, M. and Ghaly, W., "A strategy for multi-point shape optimization of turbine stages in three-dimensional flow," *ASME Turbo Expo 2009: Power for Land, Sea, and Air*, American Society of Mechanical Engineers Digital Collection, 2009, pp. 489–502.

[33]Gomes, R., Henriques, J., Gato, L., and Falcão, A., "Multi-point aerodynamic optimization of the rotor blade sections of an axial-flow impulse air turbine for wave energy conversion," *Energy*, Vol. 45, No. 1, 2012, pp. 570–580.

[34]Luo, J., Zhou, C., and Liu, F., "Multipoint design optimization of a transonic compressor blade by using an adjoint method," *Journal of Turbomachinery*, Vol. 136, No. 5, 2014.

[35]Djeddi, R. and Ekici, K., "Aerodynamic Shape Optimization Framework Based on a Novel Fully-Automated Adjoint Differentiation Toolbox," AIAA Paper 2019-3201, 2019.

[36]Djeddi, R. and Ekici, K., "Solution-based adaptive mesh redistribution applied to harmonic balance solvers," *Aerospace Science and Technology*, Vol. 84, 2019, pp. 543–564.

[37]Djeddi, R. and Ekici, K., "FDOT: A Fast, Memory-Efficient and Automated Approach for Discrete Adjoint Sensitivity Analysis using the Operator Overloading Technique," *Aerospace Science and Technology*, Vol. 91, 2019, pp. 159–174.

[38]Djeddi, R. and Ekici, K., "Novel Expression-Template-Based Automatic Differentiation of Fortran Codes for Aerodynamic Optimization," *AIAA Journal*, pp. 1–16.

[39]Spalart, P. R. and Allmaras, S. R., "A one-equation turbulence model for aerodynamic flows," AIAA Paper 1992-0439, 1992.

[40]Blazek, J., *Computational Fluid Dynamics: Principles and Applications*, Butterworth-Heinemann, Oxford, UK, 2015.

[41]Roe, P. L., "Approximate Riemann solvers, parameter vectors, and difference schemes," *Journal of Computational Physics*, Vol. 43, No. 2, 1981, pp. 357–372.

[42]Barth, T. J. and Jespersen, D. C., "The design and application of upwind schemes on unstructured meshes," AIAA Paper 1989-0366, 1989.

[43]Venkatakrishnan, V., "Convergence to steady state solutions of the Euler equations on unstructured grids with limiters," *Journal of Computational Physics*, Vol. 118, No. 1, 1995, pp. 120–130.

[44]Zhao, L. and Zhang, C., "A Parallel Unstructured Finite-Volume Method for All-Speed Flows," *Numerical Heat Transfer, Part B: Fundamentals*, Vol. 65, No. 4, 2014, pp. 336–358.

[45]Karypis, G. and Kumar, V., "A software package for partitioning unstructured graphs, partitioning meshes, and computing fill-reducing orderings of sparse matrices," *University of Minnesota, Department of Computer Science and Engineering, Army HPC Research Center, Minneapolis, MN*, 1998.

[46]Wolfe, P., "Checking the calculation of gradients," *ACM Transactions on Mathematical Software (TOMS)*, Vol. 8, No. 4, 1982, pp. 337–343.

[47]Baur, W. and Strassen, V., "The complexity of partial derivatives," *Theoretical Computer Science*, Vol. 22, No. 3, 1983, pp. 317–330.

[48]Christianson, B., "Reverse accumulation and attractive fixed points," *Optimization Methods and Software*, Vol. 3, No. 4, 1994, pp. 311–326.

[49]Christianson, B., "Reverse accumulation and implicit functions," *Optimization Methods and Software*, Vol. 9, No. 4, 1998, pp. 307–322.

[50]Mani, K., *Application of the Discrete Adjoint Method to Coupled Multidisciplinary Unsteady Flow Problems for Error Estimation and Optimization*, Ph.D. thesis, University of Wyoming, 2009.

[51]Elfarra, M. A., "Optimization of helicopter rotor blade performance by spline-based taper distribution using neural networks based on CFD solutions," *Engineering Applications of Computational Fluid Mechanics*, Vol. 13, No. 1, 2019, pp. 833–848.

[52]Byrd, R. H., Lu, P., Nocedal, J., and Zhu, C., "A limited memory algorithm for bound constrained optimization," *SIAM Journal on Scientific Computing*, Vol. 16, No. 5, 1995, pp. 1190–1208.

[53]Kraft, D., "A software package for sequential quadratic programming," *Forschungsbericht- Deutsche Forschungs- und Versuchsanstalt fur Luft- und Raumfahrt*, 1988.

[54]Economon, T., Palacios, F., and Alonso, J., "Optimal shape design for open rotor blades," AIAA Paper 2012-3018, 2012.